Earth Science Informatics (2025) 18:66
https://doi.org/10.1007/s12145-024-01657-0

RESEARCH

UAV and satellite-based prediction of aboveground biomass in scots pine stands: a comparative analysis of regression and neural network approaches

Hasan Aksoy[1] · **Alkan Günlü**[2]

Received: 2 September 2024 / Accepted: 6 December 2024 / Published online: 18 December 2024

Abstract
Forest ecosystems play a vital role in balancing the global climate through functions such as regulating carbon emissions, carbon sequestration, and energy and water cycles. Aboveground biomass (AGB) is a critical component in forest management to understand better and predict the global carbon cycle. However, traditional methods used in AGB measurement involve time-consuming, costly, and labor-intensive processes. Sentinel-1 (active), Sentinel-2, and Landsat (passive) satellite imagery, which is freely accessible and offers global coverage with frequent updates, and recently developed remote sensing platforms such as Unmanned Aerial Vehicle (UAV) serve as a valuable data source for consistent and continuous monitoring of aboveground biomass. This research focuses on modeling the relationships between AGB and data obtained from various remote sensing sources, including Sentinel-1, Sentinel-2, Landsat 8, and UAV imagery, within pure Scots pine stands in northern Türkiye. The study employs multiple linear regression (MLR) and artificial neural networks (ANNs) to establish these relationships. AGB values for each sample plot were calculated using an allometric equation. Backscatter coefficients and band brightness values were extracted from Sentinel-1 imagery, while reflectance values and vegetation indices were generated from Sentinel-2, Landsat 8 OLI, and UAV imagery. Additionally, texture features were computed for varying window sizes (3 × 3, 5 × 5, 7 × 7, 9 × 9, 11 × 11, 13 × 13, and 15 × 15) and orientations (0°, 45°, 90°, and 135°) based on data from Sentinel-2 and Landsat 8 OLI images for each sample plot. The relationships between remote sensing data and AGB were modeled using both MLR and ANN techniques. The findings revealed that the most accurate AGB estimation (R^2=0.82; RMSE = 0.35 ton ha^{-1}) was achieved using the texture variables derived from the 9 × 9 window size of Sentinel-2 imagery via the ANNs modeling approach, outperforming other image sources and MLR analysis.

Keywords UAV · ANNs · Natural forest · Forest stand metrics

Introduction

Forests play a pivotal role in global climate dynamics by serving as crucial repositories of carbon and actively regulating energy and water cycles (Herold et al. 2019; Puliti et al. 2021). Forest aboveground biomass (AGB) is an essential component of overall carbon storage, and its quantification is indispensable for the improved estimation and understanding of the intricate dynamics of the global carbon cycle, particularly within the framework of forest management plans (Santoro et al. 2021; Moradi et al. 2022). The AGB can directly reflect the primary productivity level of vegetation and significantly inform us about the benefits and drawbacks associated with the ecosystem's structure. It is an important indicator for monitoring and evaluating forest landscape dynamics and plays an important role in

Communicated by: H. Babaie

✉ Alkan Günlü
alkangunlu@karatekin.edu.tr

Hasan Aksoy
haksoy@sinop.edu.tr

1 Vocational School of Ayancık, Department of Forestry, Program of Forestry and Forest Products, Sinop University, Sinop, Turkey

2 Department of Forestry Engineering, Faculty of Forestry, Çankırı Karatekin University, 18200 Çankırı, Turkey

protecting and improving the ecological environment (Tao and Zhang 2013). Estimating AGB can be achieved through both direct and indirect methods. Direct estimations, derived from ground measurements, are recognized as the most precise approach. Nevertheless, applying this method across extensive forest areas is hindered by its impracticality, time consumption, and high costs, as noted by Vashum and Jayakumar (2012) and Moradi et al. (2022). The progression of remote sensing technology, however, offers a viable solution for the efficient and timely prediction of AGB, equipped with varying temporal and spatial resolutions, as highlighted in studies by Chen et al. (2016), Zhang et al. (2018), Pham et al. (2019), and Han et al. (2021).

Remote sensing has the potential to provide effective and rapid data for monitoring and planning forest resources in large forest areas (Dong et al. 2003; Jiang et al. 2022). It also provides the distinct advantages of speed, accuracy, minimal impact on vegetation, and the capacity to monitor large areas, setting it apart from traditional methods of biomass measurement (Issa et al. 2019; Bindu et al. 2020). In recent years, studies on reliable, low-cost aboveground biomass estimations in large areas have started to increase by combining remote sensing data with ground inventory data. A combination of optical data, light detection and ranging (LIDAR) data, synthetic aperture radar (SAR) data, and remote sensing datasets are used to enhance the prediction of AGB (Georgopoulos et al. 2022). Landsat images, the first natural resource satellite, have long been used in studies to estimate the AGB in large forest areas from past to present (Zheng et al. 2004; Günlü et al. 2014; Yavaslı and Ölgen, 2017; Ou et al. 2019; Turgut and Günlü 2022; Bulut 2023). Sentinel-2, which has better spatial resolution than Landsat, has been utilized in many studies to estimate the AGB since 2015 (Forkuor et al. 2018; Mauya et al., 2021; Bulut et al. 2022; Nuthammachot et al. 2022).

Contrary to optical satellite images, SAR images with good penetration are also used to estimate the AGB (Achard et al. 2010; Soja et al. 2015; Ban et al. 2020; Yadav et al. 2021). The SAR images have different wavelengths, such as X, C, P, and L, and, such as VV, HV, HH, and VH, different polarizations. P and L bands provide better results in estimating AGB, especially in forests with high canopy closure due to their long wavelengths (Ouchi 2013; Thapa et al. 2015; Georgopoulos et al. 2022). The LiDAR data is often used to estimate AGB due to its heavy penetration into vegetation (Lu et al. 2012; Silva et al. 2018; Zhang et al. 2023). However, there are limitations in estimating AGB in large forested areas as LIDAR data is costly to obtain and data is not spatially continuous (Listopad et al. 2011; Ehlers et al. 2022). The introduction of the Sentinel-1 C band satellite image in 2014, available for free download, has led to its prevalent usage as an active satellite image in recent research endeavors aiming to estimate AGB (Argamosa et al. 2018; Ronoud et al. 2021; Nuthammachot et al. 2022; Güvercin and Günlü, 2023). Due to the short wavelength of the image (about 6 cm), it interacts with the upper part of the stand cover (Nasirzadehdizaji et al. 2019). Recently, however, there has been a marked rise in studies focusing on the estimation of AGB through the utilization of backscattering values, texture, and polarization indices extracted from various polarizations (VV and VH) of the Sentinel-1 C band satellite imagery (Castillo et al. 2017; Chen et al. 2019; Zhang et al. 2023).

Interestingly, cost-effective and high-resolution Unmanned Aerial Vehicle (UAV) images have been used for estimating AGB, presenting a viable alternative to both active and passive satellite images (Ni et al. 2019; Ye et al. 2019; Lin et al. 2022; Basyuni et al. 2023). For example, Ni et al. (2019) and Basyuni et al. (2023) used a canopy height model with UAV image-derived DSM and DTM data and calculated tree height to estimate AGB. In another study by Ye et al. (2019), the coordinates of sample trees with their diameters at breast height were accurately determined in a small local area with UAV images to estimate AGB. Similarly, Lin et al. (2022) integrated a LIDAR camera with UAVs and calculated tree height and canopy radius with allometric equations to estimate the AGB of trees in Ma'anxi Wetland Park. In a study conducted by Wang et al. (2023), reflectance and vegetation index values obtained from UAV images were utilized to estimate AGB with various machine learning techniques such as Extreme gradient boosting (XGBoost), gradient boosting decision tree (GBDT), random forest (RF), radial basis function neural network (RBFNN), and support vector regression (SVR). However, these studies are particularly limited, as they predominantly estimate AGB using tree attributes like diameter, height, and crown diameter. Notably, these studies have not focused on estimating AGB in larger forested areas by leveraging analogous variables derived from UAV imagery.

On the other hand, both parametric and non-parametric models have been used to estimate the AGB (Huang et al. 2019). The parametric model is one of the most general prediction models due to its capability to measure the relationships between independent variables and AGB (Ou et al. 2019). Zhu et al. (2017) emphasized that the stepwise multiple linear regression (MLR) model is capable of identifying those associated with the dependent variable by considering the relationships between explanatory variables. Disregarding models that lack a substantial impact on dependent variables may result in decreased predictive accuracy regarding the relationships between independent variables and AGB (Zhao et al. 2022; Zhang et al. 2023). Various non-parametric models have been used to estimate AGB, such as artificial neural networks (ANNs) (Dong et al. 2019; Günlü et al. 2021a, b; Zhang et al. 2023), k-nearest neighbors (kNN) (Zhang et al. 2022), random forest (RF) (Li et al. 2020; Tang et al. 2022), support vector machine (SVM) (Sivasankar et al. 2013; Han et al., 2022), maximum entropy (MaxEnt) (Wang et al. 2022), extreme gradient boosting (XGBoost) (Li et al. 2020), and multivariate adaptive regression splines (MARS) (Baloloy et al. 2018). Although non-parametric models provide a perfect fit effect, it is not easy to improve the precision effect caused by underestimation and overestimation (Zhang et al. 2023). ANN stands as a prevalent non-parametric modeling technique widely used to estimate AGB (Alquraish and Khadr 2021; Wang et al. 2022; Zhang et al. 2023).

The primary objective of this study is to achieve the most accurate estimation of AGB using various modeling techniques and remote sensing data. The second aim is to investigate whether UAV imagery can serve as an alternative data source to Sentinel-1, Sentinel-2, and Landsat 8 OLI satellite imagery for AGB estimation. To facilitate comparison, feature extraction from UAV imagery was conducted in the same manner as that applied to satellite images on a sample plot basis, followed by modeling. This approach is the most significant aspect that distinguishes this study from others in the literature. Typically, AGB estimation in existing studies relies heavily on single-tree features, such as diameter and height, obtained from UAVs and LIDAR cameras integrated into UAVs. Most of these studies have been conducted in plantations or small local areas. In contrast, our study was carried out in natural forests with diverse site characteristics and stand structures. This characteristic of our research represents the second critical factor that sets it apart from other studies. The third objective of this study is to comprehensively estimate AGB by utilizing both active (Sentinel-1) and passive (Sentinel-2 and Landsat 8 OLI) remote sensing data, as well as UAV imagery, employing stepwise MLR and ANN techniques. This section aims to determine which modeling technique yields the most predictive and applicable models. To explore the potential for achieving the highest level of AGB estimation, the study investigates not only MLR and ANN modeling techniques but also examines models with varying momentum and learning rates within the ANN framework. This aspect of the research distinguishes it further from other studies in the literature.

Materials and methods

Study area

The Sinop Regional Directorate of Forestry (RDF), which is one of the 30 RDFs in Türkiye, was chosen as the study area. The study was carried out in seven different planning units within the boundaries of Sinop RDF. It is located between 34° 10′ 26″ and 35° 30′ 06″ E longitude and, 42° 05′ 30″ and 41° 20′ 30″ N latitude. The study area is located in the northernmost part of Türkiye and is covered with rich forest areas since it has precipitation around the year. The Sinop RDF has 556,275.50 ha of forested area with 7548.49 ha of pure Scots pine stands. The *Pinus nigra*, *Pinus sylvestris*, *Fagus orientalis*, *Carpinus betulus*, *Abies nordmanniana*, *Quercus infectoria*, *Quercus frainetto*, *Quercus cerris*, *Quercus petraea*, *Quercus robur*, *Juniperus sp.*, *Fraxinus excelsior*, *Ulmus L.*, *Sp.* and *Populus tremula* are the most common tree species of the forest ecosystems. The case study area experiences warm summers due to its Black Sea climate, while winters tend to be cool. The area exhibits an average annual precipitation of 685.7 mm, with an average of 2 rainy days per year. During summer, the temperature tends to peak at an average high of 35 °C, while the mean annual temperature rests at 14 °C (GDF 2020). The location of the study area and the UAV (Unmanned Aerial Vehicle) image locations related to two of the planning units are illustrated in Fig. 1. Since the study was conducted across seven different planning units and there was no opportunity to present UAV images from each unit, Fig. 1 showcases UAV images from two randomly selected planning units.

Ground measurements

In this study, a total of 184 sample plots were established, encompassing various developmental stages, crown closure levels, and site index classes. The size of the sample plots varies between 400 m^2 and 800 m^2, determined according to the stand crown closure 800 m^2 in low closed stands (11–40%), 600 m^2 in medium closed stands (41–70%), and 400 m^2 in fully closed stands (71–100%). The diameters at breast height were measured for all trees exceeding 8.0 cm in diameter at breast height in each sample plot. Field measurements were carried out in March - October 2021. The aboveground biomass (AGB) of trees in the sample plot was calculated using the allometric Eq. (1) developed by Yavuz et al. (2010) for pure Scots pine stands. Then, the AGB of each tree within the sample plots was collected, and the AGB for each sample plot was calculated. Finally, the total AGB per hectare was calculated using Eq. 2.

$$AGB = 6.89952 - 2.423793xd_{1.3} + 0.373438xd_{1.3}^{2} \tag{1}$$

AGB: aboveground biomass (single tree), $d_{1.3}$ is the tree diameter measured at 1.30 m from the ground.

$$AGB\left(tonnes\ ha^{-1}\right) = \frac{10000}{\mathrm{A}} \times AGB \tag{2}$$

AGB is the aboveground biomass (tons ha^{-1}), A is the sample plot area (m^2), and AGB is the total aboveground biomass of the sample plot (tons).

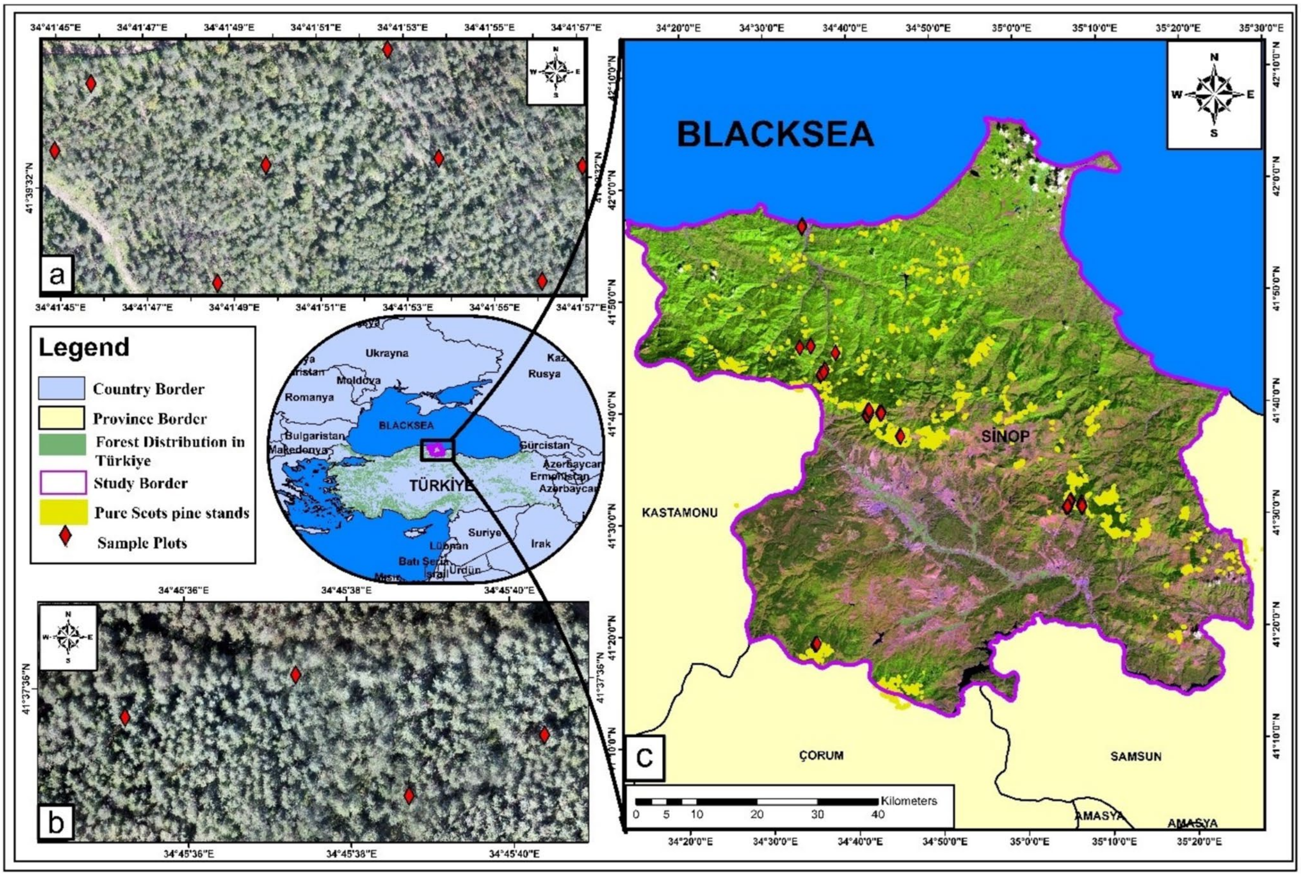

Fig. 1 The case study area (**a**) UAV flight image of Sakız planning unit (**b**) UAV flight image of Yemişli planning unit and some sample areas on UAV image (**c**) The location of Sinop Regional Directorate of Forestry in Türkiye (Landsat 8 image; bands 6, 5, 4 false-color composite)

Satellite Data and Processing

In this study, Sentinel-1, Sentinel-2, Landsat 8, and UAV images were used as remote sensing data. Sentinel-1 A (October 17th, 2021) SAR C-band image was obtained from the European Space Agency (ESA) Copernicus Access Hub, providing free access to download Sentinel images. It has a dual-polarized VV/VH image. The date of the Sentinel-1 image used in the study was chosen as a date close to the time of ground measurements. Its image was preprocessed using the SNAP software program. These stages are as follows: (i) read to image (ii) apply-orbit file (iii) thermal noise removal (iv) calibration (v) speckle-filter (vi) terrain correction (vii) linear to dB (viii) to the image. The backscattering values and band reflection values of both polarizations were used in the study. For this, each polarization was converted into a "vector" layer using ArcGIS 10.7 software. For each sample plot, the "buffer zone" was set according to the sizes of the sample plot (with a radius of 15.96 m for 800^2 m in low closed stands (11–40%), 13.82 m for 600 m^2 in medium closed stands (41–70%) and 11.28 m for 400 m^2 in fully closed stands (71–100%)). Then, the generated vector layer and the buffer zone were overlapped, and vector data suitable for the boundary of the sample plot were obtained. With vector transformation, the one-to-one inference was made according to the boundary of the sample plot, and data was obtained from all pixels corresponding to the boundary. Then, by applying zonal statistics to the layer converted to raster data, the backscattering (dB) values and digital band values of the VV and VH polarizations were obtained for each sample plot.

Sentinel-2 A level 1 C (Top of Atmosphere) image with 13 spectral bands acquired on October 15th, 2021, was downloaded and used in this study. Four of these bands have a spatial resolution of 10 m, six of them 20 m, and three of them 60 m resolution. Landsat 8 images with 11 spectral bands acquired on September 26th, 2021, were collected from the USGS Earth Explorer. Eight of these bands have a spatial resolution of 30 m, one of them 15 m, and two of them 100 m resolution. The bands with a spatial resolution of 30 m (except for band 9) were used in this study. The Sentinel-2 A and Landsat 8 images were calibrated (Atmospheric corrected) using the QGIS software 3.8.1 program and converted to reflectance images produced for each band.

During this study, high-resolution images were captured using a UAV (DJI Inspire-2 drone) at various intervals between the months of August and October. The specifications of the UAV and its camera are given in Table 1. Ground control points were meticulously established within the study area prior to the acquisition of UAV images. Global Navigation Satellite Systems (GNSS) receivers with cm sensitivity were used for this process. Then, the post-flight ground control point information was marked numerically on the captured images, and the numerical error of the image was reduced to cm precision. Before the ground measurements, flight plans were created to cover the sample plots in the study area. A sample flight plan image for a portion of the study area is given in Fig. 2.

Subsequently, for each flight plan, the take-off location of the UAV and its corresponding elevation information are extracted. As a result, the minimum flight altitude is determined by taking into account this elevation information. Considering the minimum flight altitude, the flight altitude is set at 120 m to ensure uniformity across all flight segments.

Following this process, the front and side overlap ratios of the images were determined based on the study's objectives, set as 80% and 70%, respectively. The camera angle was consistently adjusted to 90° for all flights. Flight operations were conducted with adjustments to the flight speed,

Fig. 2 UAV flight plan (Sakız forest planning unit)

Table 1 UAV and camera specifications

DJI Inspire 2		DJI Zenmuse X-5 S
Maximum take-off weight	8.82lbs (4000 g)	Micro Four Thirds sensor
Maximum flight time	Approx. 27 min (with zenzenx4s)	5.2 K video recording at 30fps and 4 K at 60fps
Operating temperature	−4° to 104 °F (−20° to 40 °C)	20.8 MP still image capture
Battery capacity	4280mAh	12.8 stops of dynamic range
Maximum speed	58 mph or 94 kph (sport mode)	12-bit raw photos
Energy	97.58Wh	20fps continuous burst shooting
Voltage	22.8 V	
Type	quadcopter	
Live view	1080p	

influenced by prevailing weather conditions. To ensure high image quality, all flights took place between 11:00 and 15:00, when cloud cover is minimal, and sunlight angle is most conducive, reducing shadows and dark areas that might otherwise affect the images. A total of 16 flight parcels were determined to cover the sample plots in the study area, and images of these parcels were taken. Pix4D software was used to create orthophoto, reflectance, digital terrain model (DTM), and digital surface model (DSM) of the UAV images. The creation of the images was carried out in three stages. First, the images taken were aligned in a coordinated manner, and image calibration processes were performed. In the second stage, tie points of the images were created. This process was used to identify the anchor points between the photos. A point cloud was formed with these points. After the dense point cloud was created in the final stage, digital Orthophoto, DTM, DSM, and reflectance maps were created (Fig. 3). The images of all plots determined in the study consist of three bands: red, green, and blue. As the fourth band, the Greeyscale (Panchromatic) band was also produced as specified in Eq. 3 (Pix4D 2022), and images consisting of a total of four bands were obtained. The flight plots used throughout the study are shown in Fig. 4.

$$\text{Grayscale} = 0.2126 \times \text{Red} + 0.7152 \times \text{Green} + 0.0722 \times \text{Blue} \tag{3}$$

Following the above process, each band of each image (Sentinel-2, Landsat 8, and UAV images) used in the study was converted into a vector layer using ArcGIS 10.7 software. In the study, the buffer tool in ArcGIS software was used to obtain sample plot sizes in the computer environment that matched the sizes of the field plots where ground measurements were conducted. During ground measurements, sample plots were set up as circular areas, with three different sizes determined according to canopy closure levels. If the canopy closure of a sample plot was between 11% and 40%, a circular plot with a radius of 11.28 m, resulting in an area of 400 m², was used. The selection criteria for the sample plots during ground measurements are explained above. The coordinates of the sample plot centers were recorded and saved in ArcGIS as a point layer. Then, using these center points as a reference, plots of the same size were generated in the computer environment by creating circles with the same radii as those used in the field using the buffer zone tool. This procedure was applied to all sample plots. For each sample plot, the buffer zone was set according to the sizes of the sample plot (with a radius of 15.96 m for 800 m^2 in low closed stands (11–40%), 13.82 m for 600 m^2 in medium closed stands (41–70%) and 11.28 m for 400 m^2 in fully closed stands (71–100%)). Then, the generated vector layer and the buffer zone were overlapped, and vector

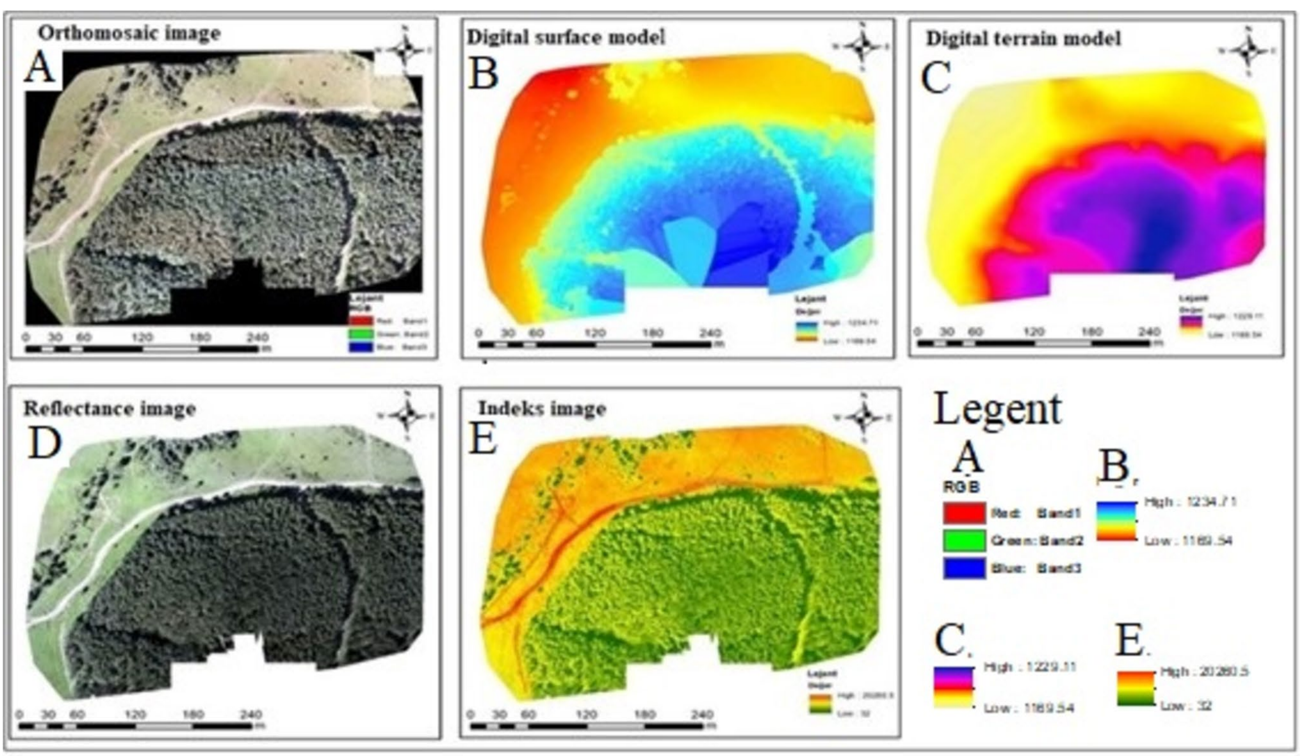

Fig. 3 Orthophoto, digital surface model, digital terrain model, reflectance, and index maps produced from UAV images (taken from Sakız planning unit with flight parcel no:1)

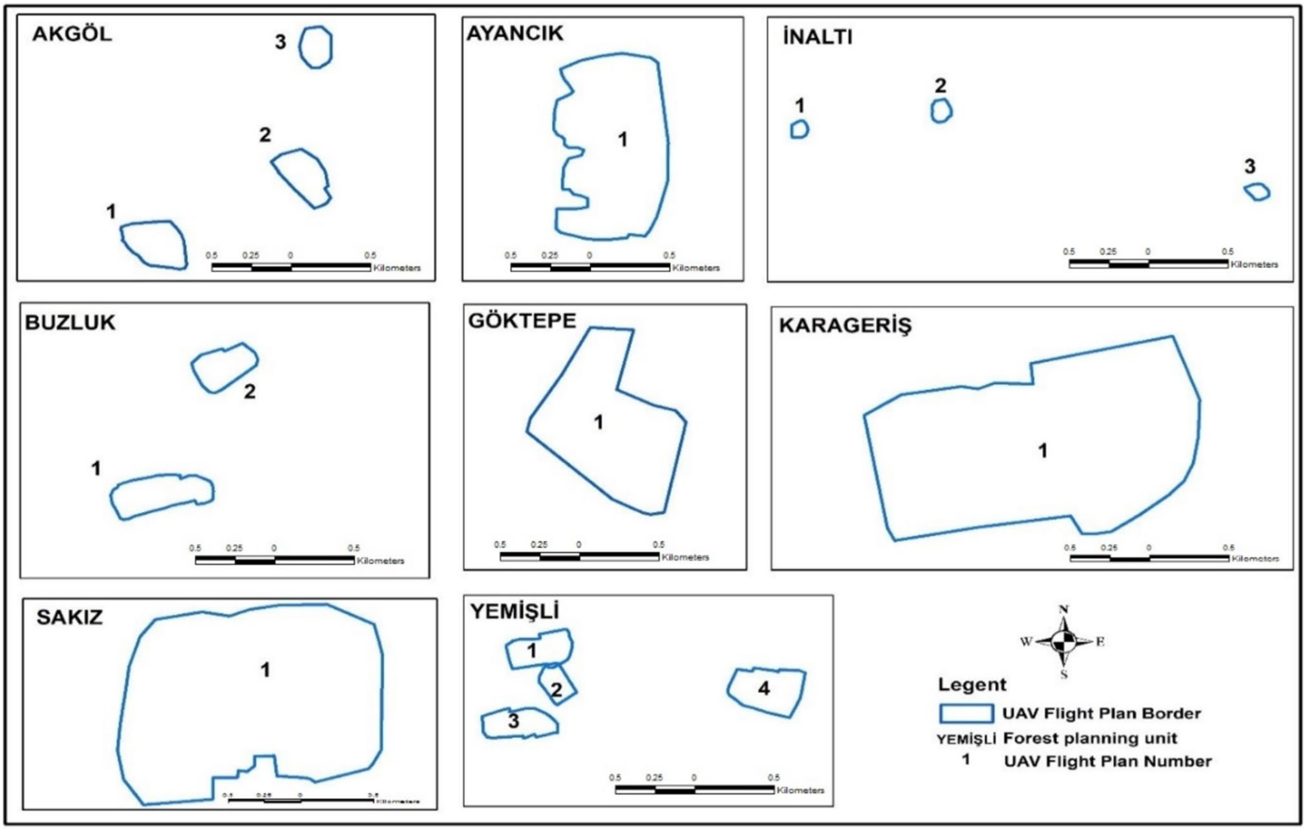

Fig. 4 Flight plots for forest planning units used in the study

data suitable for the boundary of the sample plot were created. By employing vector transformation, a one-to-one inference process was executed in accordance with the sample plot boundary, extracting data from all pixels that corresponded to this boundary. Then, the reflectance values were obtained for each sample plot by using zonal statistics to convert the layer to raster data. Utilizing the spectral bands from Sentinel-2, Landsat 8, and UAV imagery, a total of 39 vegetation indices were computed, specifically 12 from Landsat 8, 12 from Sentinel-2, and 15 from the UAV images. The vegetation indices and formulas used in the study are given in Tables 2 and 3. In addition, in this study, homogeneity (HOM), dissimilarity (DIS), correlation (COR), second moment (SM) variance (VAR), entropy (ENT), contrast (CONT) and mean (M) from Landsat 8 and Sentinel-2 satellite images were produced separately for seven different window sizes (3×3, 5×5, 7×7, 9×9, 11×11, 13×13 and 15×15) and 4 different orientations (0°, 45°, 90°, 135°). A total of 17 bands were utilized for Sentinel-2 and Landsat 8 satellite images. Thus, a total of 3808 texture data sets were created for 17 bands, 8 texture features, 7 window sizes, and 4 different orientations. The extraction of texture data involved the utilization of ENVI 5.2 software during the data acquisition process.

Modelling

During the modeling phase, data sets were prepared for modeling the relationships between aboveground biomass (AGB) obtained from ground measurements and reflectance, vegetation indices, texture features, backscattering, and digital band values obtained from Sentinel-1, Sentinel-2, Landsat 8, and UAV images. Of the 184 sample plot data used in the study, 80% (150 sample plots) were utilized in developing models, and 20% (34 sample plots) were applied in testing the models. The MLR and ANN modeling techniques were applied to the created data sets. The modeling process was performed in three stages. First of all, the AGB was estimated by MLR using remote sensing data. Secondly, predictions for the test data were obtained by using the prediction models created with the model data sets. Finally, the paired t-test was conducted to control whether there was a difference between the predictions of the test results and the observation data.

Table 2 Formulas of vegetation indices for Sentinel-2 and Landsat 8 OLI

Vegetation indices	Formulas of Landsat 8 OLI	Formulas of Sentinel 2	Reference
NDVI (Normalized Difference Vegetation Index)	(B5-B4) / (B5+B4)	(B08 - B04) / (B08+B04)	Rouse et al. (1974)
MSI (Moisture Stress Index)	(B6 / B5)	(B11 / B08)	Hunt and Rock (1989)
NBR (Normalized Burn Ratio)	(B5-B7) / (B5+B7)	(B08 - B12) / (B08+B12)	Key and Benson (2006)
EVI (Enhanced Vegetation Index)	2.5 x ((B5 – B4) / (B5+6 x B4–7.5 x B2+1))	2.5 x (B08 - B04) / ((B08+6.0 x B04–7.5 x B02)+1.0)	Liu and Huete (1995)
SAVI (Soil Adjusted Vegetation Index)	((B5 – B4) / (B5+B4+0.5)) x (1.5)	(B08 - B04) / (B08+B04+L) x (1.0+L); L=0.428	Huete (1988)
DVI (Difference Vegetation Index)	(B5 - B3) / (B5+B3)	(B08 / B04)	Tucker (1980)
GNDVI (Green Normalized Difference Vegetation Index)	(B5 - B3) / (B5+B3)	(B08 - B03) / (B08+B03)	Gitelson et al. (1996)
NDWI (Normalized Difference Water Index)	(B5 - B6) / (B5+B6)	(B08-B11) / (B08+B11)	McFeeters (1996)
MSR (Modified Simple Ratio)	((B5 / B4) –1) / $\sqrt{}$ ((B5 / B4)+1)	(B08 - B01) / (B04 - B01)	Chen (1996)
NLI (Non-Linear index)	((B5) - B4) / ((B5)+B4)	(($B08^2$) - B04)) / (($B08^2$)+B04))	Goel and Qin (1994)
PSSR (Pigment Specific Simple Ratio)	(B5 / B4)	(B08 / B04)	Blackburn (1998)
EVI2 (Enhanced Vegetation Index 2)	2.4 x (B5 - B4) / (B5+B4+1.0)	2.4 x (B08 - B04) / (B08+B04+1.0)	Jiang et al. (2008)

Table 3 Formulas of vegetation indices for UAV

Vegetation indices	Formulas	Reference	Vegetation indices	Formulas	Reference
Red-Green-Blue Vegetation Index (RGBVI)	(G x G)- (R x B)/(G x G) +(R x B)	Bendig et al. (2015)	Green–red vegetation index (GRVI)	(G – R) / (G+R)	Tucker (1979)
Green Leaf Index (GLI)	(2 x G -R- B) / (2 x G+R+B)	Louhaichi et al. (2001)	Modified green–red vegetation index (MGRVI)	(G^2- R^2) / (G^2 + R^2)	Bendig et al. (2015)
Visible Atmospherically Resistant Index (VARI)	(G-R) / (G+R-B)	Gitelson et al. (2002)	Simple blue–green ratio (BGI2)	B / G	Zarco-Tejada et al. (2005)
Normalized Green Red Difference Index (NGRDI)	(G-R) / (G+R)	Tucker (1979)	Vegetativen (VEG)	G / (R^a x $B^{(1-a)}$); a=0.667	Hague et al. (2006)
Enhanced Red-Green-Blue Vegetation Index (ERGBVE)	π x ((G^2-(R x B)) / (G^2 + (R x B))	Themistocleou (2019)	Excess green index (EXG)	2G – R- B	Woebbecke et al. (1995)
Simple red–green ratio (GR)	R / G	Gamon and Surfus. (1999)	Normalized green-blue difference index (NGBDI)	(G – B) / (G+B)	Du and Noguchi (2017)
RGB-based vegetation index 2 (RGBVI2)	(G – R) / B	García-Fernández et al. (2021)	RGB-based vegetation index 3 (RGBVI3)	(G+B) / R	García-Fernández et al. (2021)
Triangular Greenness Index (TGI)	G – 0.39 x R – 0.61 x B	Hunt et al. (2013)			

Multiple linear regression analysis

The stepwise MLR was used to model the relationships between remote sensing data and the AGB. The MLR model structure for this analysis is given below.

$$AGB = \beta_0 + \beta_1.X_1 + \beta_2.X_2 + \cdots + \beta_n.X_n + \varepsilon \quad (4)$$

The AGB was chosen as the dependent variable in the model, and the independent variables (X_1, X_2, …, X_n) were the remote sensing data obtained from Landsat 8, Sentinel-2, Sentinel-1, and UAV images; reflectance, vegetation indices, texture features, backscattering brightness and digital band values, β_0, β_1, β_2……β_n represent model coefficients, and ε is the additive bias.

Bayesian artificial neural networks

Another estimation method applied in this study is the feed-forward backpropagation Bayesian Artificial Neural Networks (BANNs) model. In this instance, a Bayesian Artificial Neural Network (BYSAM) network was designed with significant independent variables comprising reflectance, vegetation indices, texture features, backscattering, brightness, and digital band values within the AGB model, in which the MLR was applied. MATLAB codes by Bolat (2021) with different ANN model options were used in the study. However, there are some problems associated with the application of ANN. Among them, overfitting is one of the most common problems and major disadvantages encountered in neural network models. Overfitting is experienced in a way that good results in the designed network training dataset may show poor performance in the test dataset or vice versa. In fact, the overfitting problem is closely related to the number of independent variables. In general, the fit problem is inevitable for ANN models with a small training data set. One way to solve the fit problem of ANN models in this situation is to apply simple neural network models. Another way to avoid overfitting is to choose an appropriate editing training function such as Levenberg-Marquardt and Bayesian (Van Havre et al., 2015; Okut 2016; Bolat 2021; Skudnik and Jevšenak 2022).

Some parameters have been taken into account to overcome the overfitting or underfitting problems. The first step is to exercise caution and diligence in the selection process of the test dataset, which should be at a level that can represent the variability of the training dataset. During the training of this data set network, no analysis of the test data should be performed. Another important issue before the network training is determining how the data allocated as the training data set will be separated into training, testing, and validation during the network training. Retraining (in resampling) the designed network many times increases the learning capability of the network. Because the training data set is divided into different groups at each training stage, the network changes the weights of the input variables in a way that minimizes the model error value. For instance, if a 5-neuron network is trained 10 times and the average performance of the network decreases compared to the majority of the individual network performances, it indicates a good generalization ability of the network (Bolat 2021). Another issue that affects the generalization ability of the network is the training function determined for network training, as the parameter adaptations change according to the selected training function (Piotrowski et al., 2013). Bayesian network training was used in this study as its structures work in better harmony with the early stopping and regularization parameters. In ANN models, the independent variables can be normalized with different techniques to reduce the network complexity and consistency against extreme values (Akıllı and Hülya 2020). In this study, the independent variables were converted to values in the range of -1 to $+1$ using the minimum and maximum technique (Foresee and Hagan 1997). Arranging the data in the range of $[-1\ 1]$ in this network structure increases the network's generalization ability.

Another issue that affects network performance is the selection of the activation function that provides data transfer between layers. Generally, logistic sigmoid and hyperbolic tangent sigmoid functions are used to represent biological structures well with a refractive and asymptote value. In this study, the hyperbolic tangent transfer function was used since the data were arranged in the range of $[-1\ 1]$. Similarly, both learning rate and momentum value also affect network performance. The momentum value is usually chosen between 0 and 1. The learning rate is an important parameter in the network's training process. While a small learning rate causes the network to overfit the data, a large learning rate can lead to less learning and, therefore, big mistakes (Lawrence et al. 1997). Thus, determining the learning rate and momentum coefficient simultaneously is essential in improving network performance (Bolat 2021). In this study, based on the learning rate and momentum values, a total of 17 models were generated, 9 models in which the learning rate is kept constant at 0.1 and the momentum is changed between 0.1 and 0.9, and 8 models where the momentum ratio is kept constant at 0.1. The learning rate varies between 0.1 and 0.9. Among 17 models, the performance criteria and compliance status were evaluated, and the model with the highest success was chosen to represent the network.

Model performance criteria

Various indicators such as the adjusted coefficient of determination (R^2_{adj}), mean absolute error (MAE), root mean square error (RMSE), the bias (Bias), akaike's information criterion (AIC) and bayesian information criterion (BIC) criteria were used to evaluate the model success. The desired performance outcome is to have MAE, RMSE, AIC, and BIC values approaching 0 while aiming for an R^2_{adj} value close to 1. Taking into account the performance criteria calculated for AGB, a method that proves effective based on one criterion might not fare well according to another criterion's valuation. To address this concern, a comprehensive success ranking was devised to encompass all relevant success criteria. To achieve this, the approach outlined by Poudel and Cao (2013), known as the Relative Ranking Method (Ri), was adopted. Within this method, models were ranked relative to their proximity and divergence concerning the success criteria. By gathering relative sequence numbers corresponding to various criterion values, the model exhibiting the lowest total relative sequence number was identified as the most successful for AGB (Özdemir 2018; Ercanlı et al. 2018). The formulas for these statistical values are as follows (cf. Equations 5–11).

$$R^2_{adj} = 1 - \frac{(n-1)\sum_{i=1}^{n}(y_i - \hat{y}_i)^2}{(n-p)\sum_{i=1}^{n}(y_i - \bar{y}_i)^2} \tag{5}$$

$$MAE = \frac{1}{n}\sum_{i=1}^{n}|y_i - \hat{y}_i| \tag{6}$$

$$RMSE = \sqrt{\frac{1}{n}\sum_{i=1}^{n}(y_i - \hat{y}_i)^2} \tag{7}$$

$$Bias = \frac{\sum_{i=1}^{n}(y_i - \hat{y}_i)}{n} \tag{8}$$

$$AIC = \ln(RMSE) + 2k \tag{9}$$

$$BIC = \ln(RMSE) + \ln(k) \tag{10}$$

$$R_i = 1 + \frac{(\mathrm{m}-1)(S_i - S_{min})}{S_{max} - S_{min}} \tag{11}$$

Where n is the number of observations, p is the number of parameters, y_i is measured the AGB (ton ha^{-1}), $\hat{y}_i$ is predicted AGB (ton ha^{-1}), $\bar{y}_i$ is a mean of measured AGB values, k is the number of coefficients. R_i is the relative rank of method i (i = 1,2, 3,.......m), S_i is the goodness of fit statistics generated from methods, S_{min} is the minimum value of S_i, and S_{max} is the maximum value of S_i. The flow chart of the methodology used in the study is shown in Fig. 5.

Results

Multiple Linear regression analysis

Table 4 presents the success criterion values and the total rank order numbers of the relationships between AGB and remote sensing data as revealed by the multiple regression (MLR) analysis. The models obtained with the data set having the lowest total relative rank were identified as the most successful ones. The highest success with reflectance data was achieved for the Sentinel-2 satellite image (R^2_{adj} = 0.47), while the lowest success was found for the UAV image (R^2_{adj} = 0.29). The highest success with vegetation indices was achieved for the Landsat 8 (R^2_{adj} = 0.53), while the lowest success was found for the UAV image (R^2_{adj} = 0.38). When examining the model results obtained for texture features from Landsat 8 and Sentinel-2 images using the window sizes, the highest success was achieved for the 9 × 9 window size of the Sentinel-2 image (R^2_{adj} = 0.81), while the lowest success was observed for the 5 × 5 window size of the Sentinel-2 image (R^2_{adj} = 0.77). In terms of texture features, the highest success was achieved at 135^0 for the Landsat 8 (R^2_{adj} = 0.74), while the lowest success was observed at 90^0 for the Sentinel-2 (R^2_{adj} = 0.74). The success levels of the models obtained from the backscatter and digital number values of the Sentinel-1 image have turned out to be quite low. However, no significant model has been identified for the UAV digital number data in this context.

When examining the success criteria of the applied MLR model, the highest success in remote sensing datasets was achieved with texture datasets. Especially diversifying the dataset in terms of different window and orientation sizes has significantly contributed to the success of the model results. Using different window sizes, the highest coefficient of determination for aboveground biomass was obtained with texture features from the Sentinel-2 image at a window size of 9 × 9 (R^2_{adj} = 0.81) (Table 5). Prediction and observation graphs for the MLR models applied to the model-test datasets are presented in Fig. 6.

Artificial neural networks

Remote sensing datasets that provided the highest success for AGB in regression models (Table 5) were also used to obtain predictions using the Bayesian Artificial Neural Network Model (BYANNM). The utilization of diverse learning rates and momentum variables in the models led to the development of a comprehensive set of 17 models for estimating AGB (Table 6). Upon a closer examination

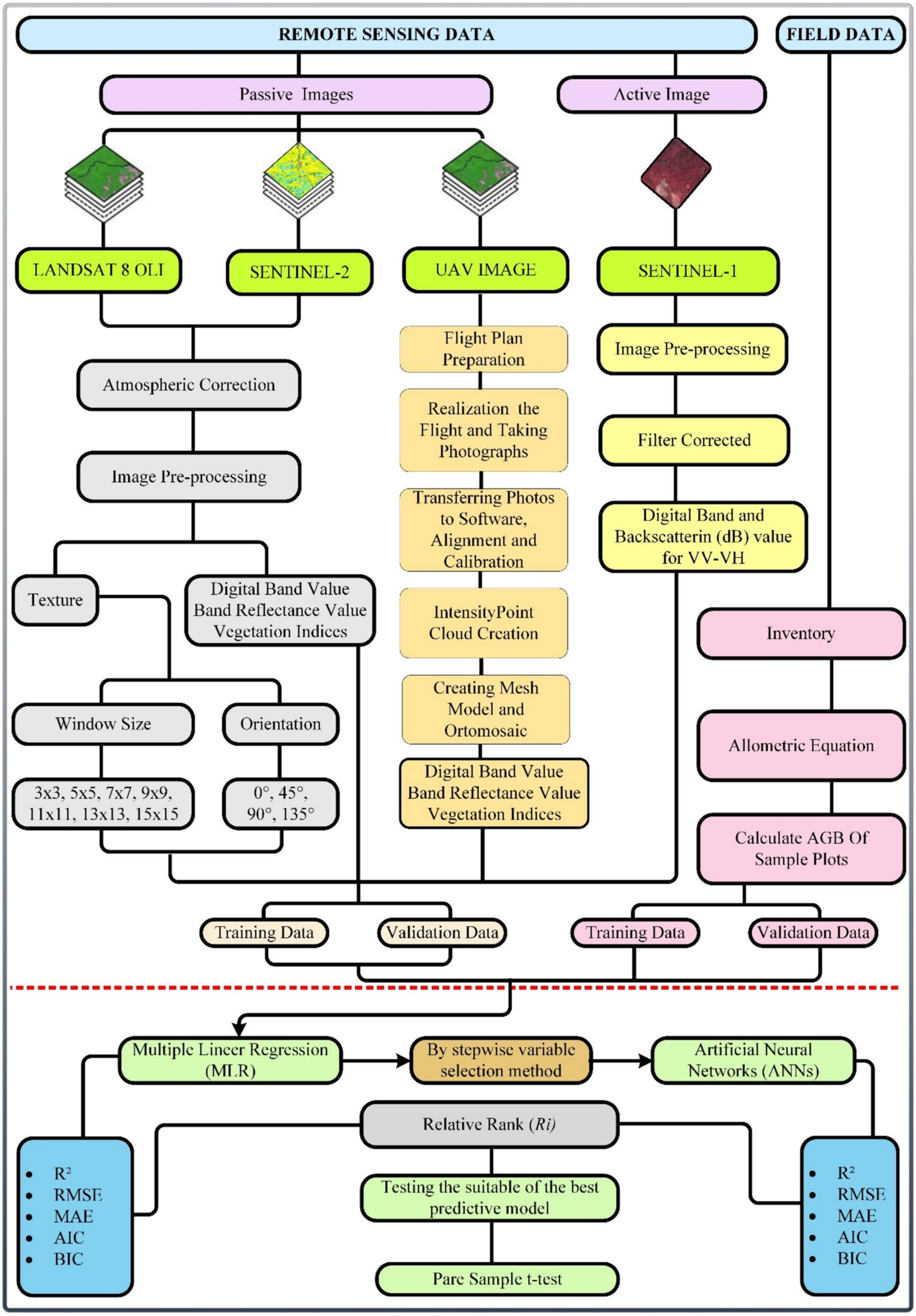

Fig. 5 Flowchart of the methodology of the study

Table 4 Success criterion values and total relative values for multiple linear regression analysis

DATASET	TRAINING					TRAINING RELATIVE RANK					
	R^2	RMSE	MAE	BIC	AIC	R^2	RMSE	MAE	BIC	AIC	Total
UAV DN	-	-	-	-	-	-	-	-	-	-	-
UAV VIs	0.38	65.13	54.46	4.87	8.18	17.93	25.40	24.32	31.00	5.27	103.92
UAV RV	0.29	69.69	56.34	4.24	6.24	21.26	27.12	25.13	27.34	3.99	104.84
Landsat 8 OLI VIs	0.53	0.55	0.46	0.51	8.41	12.31	1.09	1.10	5.46	5.43	25.39
Landsat 8 OLI RV	0.52	0.55	0.46	1.02	9.41	12.35	1.09	1.11	8.44	6.09	29.07
Landsat 8 OLI Orientation (0°)	0.75	0.39	0.31	1.46	21.06	4.00	1.03	1.04	11.03	13.84	30.94
Landsat 8 OLI Window Size (11×11)	0.77	0.38	0.31	1.32	19.02	3.25	1.02	1.04	10.25	12.48	28.04
Landsat 8 OLI Window Size (13×13)	0.81	0.34	0.21	1.33	20.93	1.82	1.01	1.00	10.27	13.75	27.85
Landsat 8 OLI Orientation (135°)	0.74	0.40	0.32	1.28	17.08	4.26	1.03	1.04	9.96	11.19	27.49
Landsat 8 OLI Window Size (15×15)	0.78	0.36	0.28	1.29	18.99	2.69	1.02	1.03	10.06	12.46	27.25
Landsat 8 OLI Window Size (3×3)	0.67	0.45	0.38	1.40	17.20	6.96	1.05	1.07	10.69	11.27	31.04
Landsat 8 OLI Orientation (45°)	0.71	0.41	0.33	1.68	25.12	5.34	1.04	1.05	12.35	16.53	36.31
Landsat 8 OLI Window Size (5×5)	0.66	0.46	0.39	1.17	13.23	7.37	1.05	1.07	9.35	8.63	27.48
Landsat 8 OLI Window Size (7×7)	0.70	0.43	0.35	1.45	19.15	5.83	1.04	1.06	11.00	12.57	31.50
Landsat 8 OLI Window Size (9×9)	0.80	0.35	0.29	1.51	24.95	2.20	1.01	1.03	11.35	16.42	32.01
Landsat 8 OLI Orientation (90°)	0.82	0.32	0.26	1.99	44.85	1.41	1.00	1.02	14.12	29.65	47.20
Sentinel 1 DN	0.03	0.78	0.66	−0.25	1.75	31.00	1.17	1.19	1.04	1.00	35.41
Sentinel 1 dB	0.07	0.78	0.65	−0.25	1.75	29.24	1.17	1.19	1.00	1.00	33.60
Sentinel 2 VIs	0.58	0.51	0.42	1.12	11.33	10.25	1.07	1.09	9.06	7.37	28.85
Sentinel 2 RV	0.47	0.58	0.48	0.56	5.46	14.45	1.10	1.12	5.77	3.47	25.90
Sentinel 2 Orientation (0°)	0.76	0.38	0.31	1.59	25.02	3.47	1.02	1.04	11.78	16.47	33.79
Sentinel 2 Window Size (11×11)	0.78	0.37	0.29	0.94	23.00	2.61	1.02	1.03	8.01	15.12	27.79
Sentinel 2 Window Size (13×13)	0.80	0.36	0.28	1.05	18.97	2.20	1.01	1.03	8.62	12.45	25.31
Sentinel 2 Orientation (135°)	0.65	0.45	0.35	1.78	25.21	7.52	1.05	1.06	12.89	16.60	39.11
Sentinel 2 Window Size (15×15)	0.83	0.32	0.25	1.50	16.86	1.00	1.00	1.02	11.25	11.04	25.31
Sentinel 2 Window Size (3×3)	0.81	0.34	0.28	1.62	28.91	1.79	1.01	1.03	11.98	19.06	34.86
Sentinel 2 Orientation (45°)	0.69	0.42	0.35	2.03	35.13	6.13	1.04	1.06	14.35	23.19	45.77
Sentinel 2 Window Size (5×5)	0.77	0.38	0.31	1.92	35.03	3.17	1.02	1.04	13.73	23.12	42.09
Sentinel 2 Window Size (7×7)	0.78	0.37	0.29	0.94	18.00	2.65	1.02	1.03	8.02	11.80	24.52
Sentinel 2 Window Size (9×9)	***0.81***	***0.35***	***0.28***	***1.14***	***16.94***	***1.82***	***1.01***	***1.03***	***9.14***	***11.10***	***24.10***
Sentinel 2 Orientation (90°)	0.80	0.33	0.25	2.06	46.88	1.86	1.00	1.02	14.55	31.00	49.44

of Table 6, it becomes evident that the model denoted as AGB8 emerged as the most suitable one based on its coefficient of determination and the cumulative relative rank number (Model $R^2 = 0.82$, Test $R^2 = 0.75$, learning rate = 0.1, momentum = 0.8, Rj = 56.22). However, there is a prevailing concern regarding overfitting in the remaining models, except for AGB5, AGB7, and AGB8 models. The graph depicting the model and test coefficients of determination for AGB is shown in Fig. 7.

Prediction and observation graphs for the ANNs applied to the model-test datasets are presented in Fig. 8, and the prediction and observation performance metrics for the models are provided in Table 7.

Furthermore, a "paired t-test" was exercised to determine whether the test predictions for the methods were consistent with the observation data. According to the test results, it was observed that the models can be used in the study area at a 0.05 significance level. Performance metrics (R^2, RMSE, MAE, BIC, AIC, BIAS) for all predictions obtained through modeling techniques and the results of the paired t-test are provided in Table 7.

Discussion

The evaluation of the results from the study revealed that the most successful model for AGB was achieved using MLR, with the model incorporating texture variables from the 9×9 window size derived from Sentinel-2 imagery (Model R^2 = 0.81, Test R^2 = 0.84). Similarly, the ANN modeling technique demonstrated a high level of success (Model R^2 = 0.82, Test R^2 = 0.75) (Table 6). The p-values

Table 5 Above ground biomass model obtained with 9×9 window size texture data from Sentinel-2 image

Independent variables	Coefficients of Independent Variables	t statistics	*p*-value
Constant	3.815	7.098	0.000
M_S12_9_45°	0.280	3.472	0.001
CON_S5_9_0°	−1.525	−2.278	0.024
CON_S8A_9_0°	0.621	4.691	0.000
CON_S5_9_45°	0.812	5.531	0.000
CON_S5_9_135°	0.262	2.777	0.006
COR_S5_9_135°	0.501	2.586	0.011
M_S7_9_45°	−0.459	−6.875	0.000
M_S7_9_0°	0.458	5.709	0.000
DIS_S11_9_0°	−0.975	−3.218	0.002
CON_S8_9_135°	1.080	4.206	0.000
SM_S12_9_90°	0.914	2.157	0.033
HOM_S7_9_90°	1.469	3.330	0.001
DIS_S8_9_135°	−1.810	−3.058	0.003
CON_S6_9_0°	−0.947	−2.100	0.038

from the paired t-test for the test data of both methods were 0.346 for MLR and 0.981 for ANNs, indicating no significant difference between the models (Table 7). However, the MLR test displaying a higher R2 value compared to the model, coupled with the t-test revealing a lower p-value than that of ANNs, strongly indicates that ANN is the more appropriate and preferable option for AGB estimation. The results obtained from the study have been discussed separately below for each of the four different images, in conjunction with some studies from the literature on the topic.

Landsat 8 OLI Satellite Image

The study modeled the relationships between AGB and band reflectance, vegetation indices, and texture variables obtained from Landsat 8 OLI satellite imagery using the Multiple Linear Regression (MLR) modeling technique. The best R^2 values were 0.52 for the model using reflectance variables, 0.53 for vegetation indices, and 0.80 for texture variables (see Table 4). When the studies on the subject in the literature are examined, Lu (2005) modeled the variables obtained from Landsat TM imagery using MLR, with the highest R^2 value achieved by the model using band reflectance variables. Similar results were found in the study conducted by Turgut and Günlü (2022). Turgut and Günlü (2022) used MLR to model AGB in pure Crimean pine stands, employing vegetation indices and band reflectance variables derived from Landsat 8 data. The analysis of the results revealed that the model using band reflectance values as the independent variable ($R^2 = 0.445$) outperformed the model using vegetation indices ($R^2 = 0.387$). Contrary to this, a study conducted by Gaspari et al. (2010) used Landsat 7 ETM + satellite imagery to model AGB, and they found that the model using vegetation indices provided a higher R^2 value compared to other variables. Another study conducted by Günlü et al. (2014) in pure Crimean pine forests in Turkey used MLR to model the relationships between vegetation indices and band reflectance values from Landsat TM and AGB. The study found that vegetation indices ($R^2 = 0.606$) provided more accurate results than band reflectance values ($R^2 = 0.465$). Bulut (2023) used MLR to model the relationships between band reflectance, vegetation indices obtained from Landsat 8, and AGB in pure Calabrian pine stands. The study demonstrated that vegetation indices were more effective than band reflectance variables in predicting

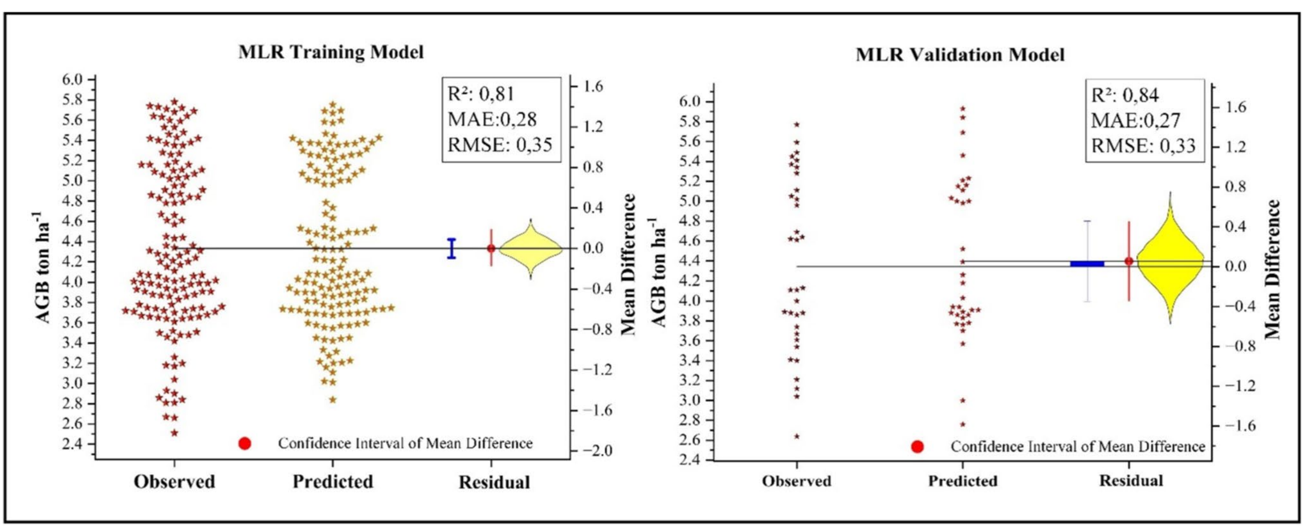

Fig. 6 Observation, prediction, and error distribution graph according to the multiple linear regression model (for both model and test)

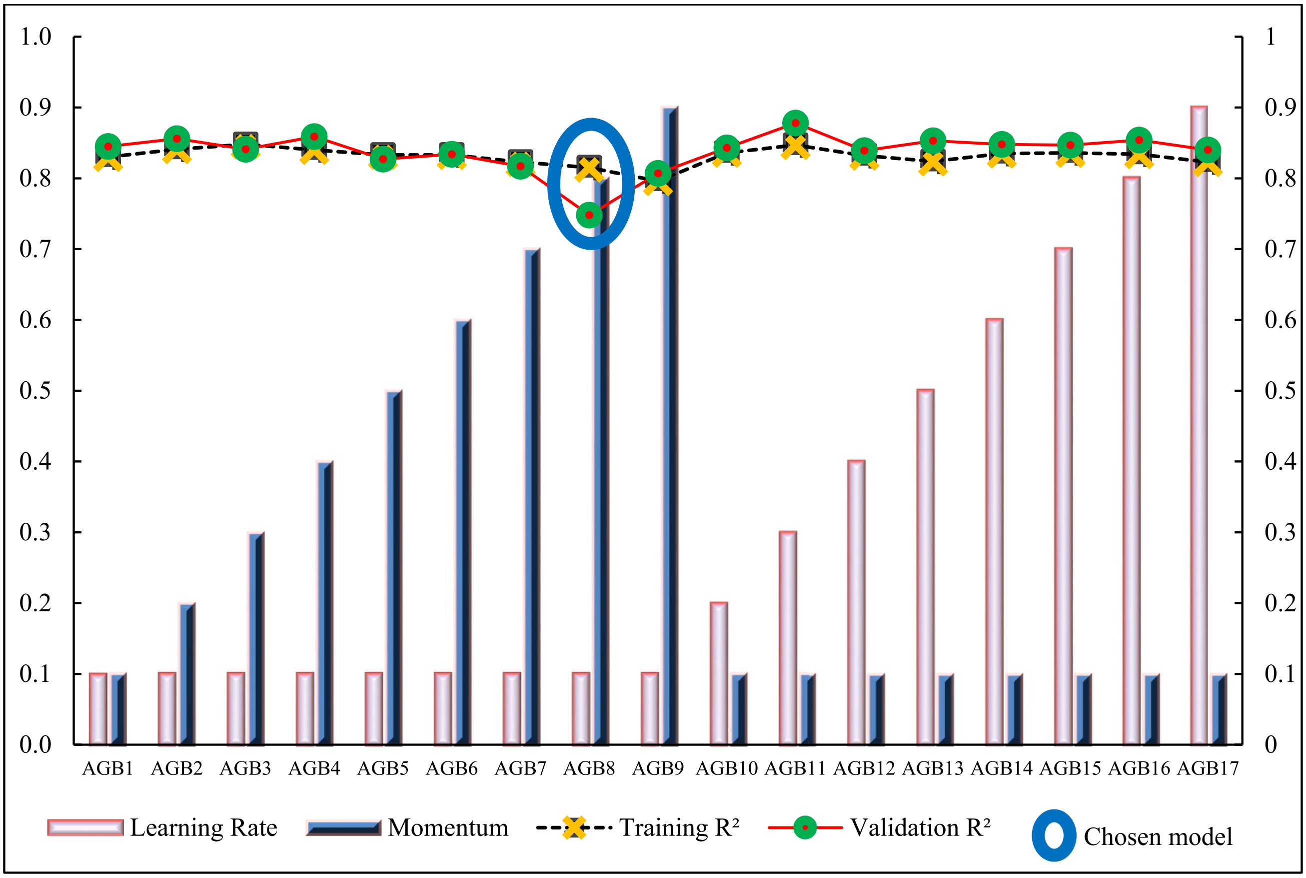

Fig. 7 Graph illustrating the coefficient of determination for the estimation of aboveground biomass employing the BYANNM method

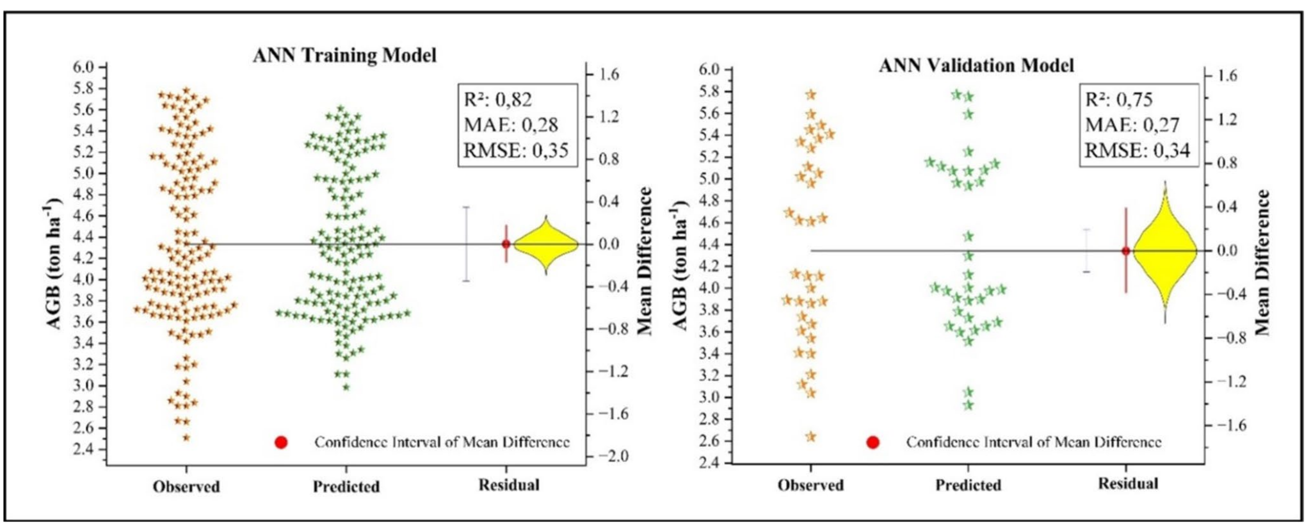

Fig. 8 Observation, prediction, and error distribution graph according to the ANNs model (for both training and testing)

AGB. In studies that used band reflectance and vegetation index variables derived from satellite imagery to predict AGB, vegetation indices generally yielded more successful results. This is because vegetation indices are generally more effective in predicting AGB due to their ability to capture the condition of green vegetation with greater sensitivity. However, vegetation indices can also help mitigate the effects of environmental conditions and shadows on reflectance,

Table 6 Success criterion values and total relative values for ANNs

Model No	Parameters						Training						Validation					
	Lr.	Mo.	Input	Output	Hl.	Neuron	R^2	RMSE	MAE	BIC	AIC	Total Relative Rank	R^2	RMSE	MAE	BIC	AIC	Total Relative Rank
AGB1	0.1	0.1	14	1	1	2	0.83	0.33	0.27	1.54	26.90	35.85	0.85	0.34	0.27	1.55	26.91	44.12
AGB2	0.1	0.2	14	1	1	2	0.84	0.32	0.25	1.50	26.86	15.34	0.86	0.32	0.25	1.51	26.87	29.66
AGB3	0.1	0.3	14	1	1	2	0.85	0.31	0.25	1.48	26.84	5.98	0.84	0.34	0.28	1.56	26.92	47.85
AGB4	0.1	0.4	14	1	1	2	0.84	0.32	0.26	1.51	26.87	19.89	0.86	0.32	0.27	1.51	26.87	32.55
AGB5	0.1	0.5	14	1	1	2	0.83	0.33	0.26	1.53	26.89	30.10	0.83	0.35	0.28	1.60	26.96	60.96
AGB6	0.1	0.6	14	1	1	2	0.83	0.33	0.26	1.53	26.89	31.08	0.83	0.35	0.28	1.58	26.94	55.13
AGB7	0.1	0.7	14	1	1	2	0.82	0.34	0.28	1.56	26.92	47.23	0.82	0.36	0.29	1.63	26.99	70.71
AGB8	0.1	0.8	14	1	1	2	0.82	0.35	0.28	1.58	26.94	56.22	0.75	0.34	0.27	1.55	26.91	56.29
AGB9	0.1	0.9	14	1	1	2	0.80	0.37	0.30	1.63	26.99	85.00	0.81	0.35	0.31	1.58	26.94	66.34
AGB10	0.2	0.1	14	1	1	2	0.84	0.33	0.26	1.52	26.88	24.68	0.84	0.34	0.27	1.55	26.91	44.59
AGB11	0.3	0.1	14	1	1	2	0.85	0.32	0.25	1.48	26.84	6.30	0.88	0.30	0.25	1.42	26.78	5.00
AGB12	0.4	0.1	14	1	1	2	0.83	0.33	0.27	1.53	26.89	32.37	0.84	0.34	0.28	1.56	26.92	50.17
AGB13	0.5	0.1	14	1	1	2	0.82	0.34	0.27	1.56	26.92	45.33	0.85	0.33	0.27	1.52	26.88	37.28
AGB14	0.6	0.1	14	1	1	2	0.84	0.33	0.26	1.52	26.89	28.22	0.85	0.33	0.27	1.54	26.90	40.26
AGB15	0.7	0.1	14	1	1	2	0.84	0.33	0.25	1.52	26.88	22.06	0.85	0.33	0.25	1.54	26.90	37.83
AGB16	0.8	0.1	14	1	1	2	0.83	0.33	0.26	1.52	26.89	27.87	0.85	0.33	0.26	1.52	26.88	32.95
AGB17	0.9	0.1	14	1	1	2	0.82	0.34	0.27	1.56	26.92	45.27	0.84	0.34	0.27	1.56	26.92	47.27

Lr: Learning Rate, Mo: Momentum, Hl: Hidden Layer, AGB1: Aboveground biomass 1st model

Table 7 Model performance values obtained from 9×9 filtered texture data of Sentinel-2 image for AGB

	Method	R^2	RMSE	MAE	BIC	AIC	BIAS	Paired *t-test*	
								t	*p value*
Training	MLR	0,81	0,35	0,28	1,14	16,94	$-5{,}56\times10^{-15}$		
	ANN	0,82	0,35	0,28	1,58	26,94	$3{,}05\times10^{-15}$		
Validation	MLR	0,84	0,33	0,27	1,54	26,90	$6{,}11\times10^{-15}$	−0,956	0,346
	ANN	0,75	0,34	0,27	1,55	26,91	$4{,}27\times10^{-15}$	0,024	0,981

thereby improving the correlation between AGB and vegetation indices, especially in forest ecosystems with complex vegetation cover (Lu 2005).

In the study, the best model performance was achieved using texture variables from the Landsat 8 OLI satellite. A review of the literature reveals that similar results have been obtained in studies comparable to ours. The study by Dube and Mutanga (2015) estimated the relationships between AGB and variables such as band brightness values, vegetation indices, and texture features derived from Landsat 8 OLI satellite imagery. The findings indicated that texture features were the most effective predictors of AGB, achieving an R^2 of 0.76. Ou et al. (2019) predicted AGB in *Pinus densata* forest areas using Landsat 8 OLI data. The study concluded that texture features derived from Landsat 8 OLI images contributed more to improving prediction accuracy than the original spectral band values. Texture features are independent of an object's surface color and brightness, capturing the frequency of changes within a specified window size. This sensitivity to canopy structure allows for detailed differentiation of vegetation and the detection of diverse forest canopy characteristics (Zhang et al. 2020). Texture features play a critical role in enhancing the predictive accuracy of AGB models. However, identifying texture features that exhibit strong correlations with AGB remains essential. Selecting the most suitable texture features for AGB prediction is challenging, as these features can vary depending on forest stand structures and the satellite imagery used in the study area. This selection process also involves determining optimal window sizes and orientation, selecting appropriate image bands (Chen et al. 2004; Eckert 2012; Barbosa et al. 2014). In our study, the best model performance for the Landsat image was achieved with a window size of 9×9 and an orientation of 0^o. (see Table 4). A review of some studies in the literature on texture features derived from satellite images for predicting AGB shows that variables with different window sizes and orientations have been included in the models. In the study by Turgut and Günlü (2022), texture variables with window sizes of 3×3, 5×5, 7×7, and 9×9 from different bands were included in the model for predicting AGB and the model's performance was found to be 0.552. In the study by Phua et al. (2017), variables with window sizes of 3×3 and 5×5 were included in the model for AGB modeling, and the model's performance was found to be 0.52. Persson's (2016) study showed that the best results for estimating AGB were obtained with an 11×11 window size. Maack et al. (2015) found that a 3×3 window size provided the best prediction for AGB. In a study conducted by Bulut et al. (2023) on predicting forest stand parameters, they found the best model results for predicting these parameters at different orientations (45, 90, and 135^o). When reviewing studies related to the topic in the literature, some of which are mentioned above, due to the limited research on predicting stand parameters using textural features derived from satellite images, there is a lack of clarity regarding the optimal orientation and window size. It is not fully understood how to determine the appropriate values for the moving window size and orientation when considering textural features. In recent years, various machine-learning techniques have been used to estimate AGB. A review of related studies in the literature shows that, as in our study, machine learning techniques have yielded more successful results compared to MLR. Safari et al. (2017) attempted to estimate the AGB using multivariate adaptive regression splines (MARS), random forest (RF), boosted regression trees (BRT), and support vector machine (SVM) modeling techniques with raw band, raw band ratios and vegetation indices obtained from Landsat 8 data. They indicated that model success varied according to variables and modeling techniques. In another study by Li et al. (2019a, b), the AGB was estimated using Landsat 8 imagery in four different vegetation types using MLR, improved back-propagation neural network (Improved BBPNN), and SVM techniques. The results of the study showed that the success levels obtained from different modeling techniques varied for different vegetation types. In coniferous forests, for instance, the most effective model was derived using MLR, whereas in broadleaf forests, the SVM modeling technique produced the best model. Comparable results were also identified in our study. In the study conducted by Günlü et al. (2021a, b), the relationships between band reflectance, vegetation indices, and texture features obtained from Landsat 8 OLI images and AGB were modeled using MLR and ANN. Upon reviewing the results, it was found that the ANN method provided more successful results than the MLR method for all variables. Similar results have been found in the studies conducted by Xu et al. (2011), López-Serrano et al. (2016), Sakıcı and Günlü (2018), Bulut (2023), and Anees et al. (2024).

Sentinel-2 Satellite Image

The study utilized the Multiple Linear Regression (MLR) technique to model the relationships between AGB and various predictors, including band reflectance, vegetation indices, and texture variables derived from Sentinel-2 satellite imagery. The highest R^2 values achieved were 0.47 for models using reflectance variables, 0.58 for vegetation indices, and 0.81 for texture variables (see Table 4). For Artificial Neural Networks (ANN), the best performance was observed with Model 8, achieving a success rate of 0.82 (see Table 6). When the studies in the literature related to the topic are examined, Muhe and Argaw (2022) examined the relationship between AGB and band reflectance and vegetation indices values obtained from Sentinel-2 imagery using correlation analysis and found the best correlation with AGB in vegetation indices. In the investigation carried out by Ahmad et al. (2023), the associations between vegetation indices and band reflectance variables retrieved from Sentinel-2 were scrutinized concerning AGB in moist temperate forests. MLR was employed, revealing that the best model outcomes were achieved with the vegetation indices. In the study conducted by Anish et al. (2022), above-ground carbon was estimated using vegetation indices calculated from Sentinel-2 satellite imagery, and the R^2 was found to be 0.76. Muhe and Argaw (2022) examined the relationship between AGB and band reflectance and vegetation indices values obtained from Sentinel-2 imagery using correlation analysis and found the best correlation with AGB in vegetation indices. Similar to Ahmad et al. (2023), the associations between vegetation indices and band reflectance variables retrieved from Sentinel-2 were scrutinized concerning AGB in moist temperate forests. MLR was employed, revealing that the best model outcomes were achieved with the vegetation indices. In the study conducted by Li et al. (2021), the best model performance for predicting AGB was achieved using texture variables derived from Sentinel-2 satellite imagery with a 7×7 window size. Unlike our study, the study conducted by Li et al. (2021) reported better model performance with medium window sizes (5×5 and 7×7). Our study achieved the best model performance with a window size of 9×9 and an orientation of 0°. In the study conducted by Demirel et al. (2023) on pure cedar stands, the relationships between aboveground carbon and band reflectance and vegetation indices derived from Sentinel-2 satellite imagery were modeled. When the results were examined, similar to our study, a higher model determination coefficient (0.448) was achieved with vegetation indices. Unlike our study, the study conducted by Keleş et al. (2021) found that in predicting aboveground carbon, band reflectance variables (0.265) performed slightly better than vegetation indices (0.244) in terms of model results. In the study conducted by Bulut et al. (2023), texture variables derived from Sentinel-2 satellite imagery with different window sizes and orientations were used to predict stand parameters such as stand volume, basal area, number of trees, and dominant height. The best model determination coefficient was 0.82 for the number of trees at 45°, 0.79 for stand volume, 0.72 for basal area at 90°, and 0.72 for dominant height at 135°.When evaluated in terms of window size, they found that the R2 was 0.74 for stand volume with 7×7 and 9×9 window sizes, 0.71 for basal area with a 7×7 window size, 0.80 for tree count with a 7×7 window size, and 0.70 for dominant height with a 9×9 window size. When reviewing the literature, it has been found that similar to the model performance obtained from Landsat 8 satellite imagery, the best model performance for Sentinel-2 satellite imagery was also achieved using texture variables. Texture features offer insights into the horizontal structure, spatial variation, and relative gray value distribution within an image, which helps in identifying ground objects or regions of interest (Kelsey, 2014). They have been suggested as a solution to the problem of vegetation index saturation in areas with high biomass density. Texture analysis is widely applicable to remote sensing imagery and presents a promising method for improving the accuracy of biomass modeling at both local and regional scales (Sarker and Nichol 2011; Sibanda et al. 2017). The window sizes and orientations of texture features have a significant impact on AGB prediction. However, it is not yet clear which specific window size and orientation of texture features are most effective in predicting AGB and other stand parameters (Li et al. 2021). As mentioned above, when reviewing the literature for Landsat 8 imagery, it has been observed that machine learning techniques, when applied to variables derived from Sentinel-2 satellite imagery, provided more successful model results in modeling the relationships between AGB compared to the MLR method (Wan et al. 2018; Li et al. 2019a, b; Keleş et al., 2021; Quang et al. 2022; Zhang et al. 2024; Nguyen et al.,2024).

Sentinel-1 Satellite Image

This study revealed exceedingly weak correlations between the variables obtained from the Sentinel-1 satellite image and AGB (Table 4). Similar results were found in different studies in the literature (Nuthammachot et al. 2022; Güverçin and Günlü 2023a, b). While C-band Sentinel-1 provides high spatial resolution synthetic aperture radar (SAR) data, it is not sufficient to estimate the AGB due to the low penetration and saturation point (Gasparri et al. 2010; Li et al. 2020). It does not reach the ground due to short wavelengths with backscattering from the upper layer of the stand (Quegan et al. 2019; El Hage et al. 2022). However, when reviewing the literature, it becomes apparent that various studies have focused on estimating AGB by analyzing variables derived from Sentinel-1 C alongside parameters such as band reflectance, vegetation indices, and texture values obtained from passive satellite imagery like Landsat and Sentinel-2. These studies indicated that the model's success in estimating AGB significantly improved when combining Sentinel-1 C data with other passive satellite imagery compared to relying solely on Sentinel-1 C data (Zhang et al. 2015; Wang et al. 2019; Nuthammachot et al. 2022). In examining the literature further, Kumar et al. (2016a, b) estimated AGB by MLR using Landsat 8 and ALOS-2 images separately. Relationships were found at the level of model success ($R^2 = 0.788$) with the variables of the Landsat 8 image and ($R^2 = 0.742$) with the variables of the ALOS-2 image. It was observed, however, that the model success increased when the variables obtained from both satellite images were used together ($R^2 = 0.859$). Nuthammachot et al. (2022) tried to estimate AGB by utilizing variables derived from Sentinel-2 and Sentinel-1 images separately as well as in conjunction with each other. Upon analyzing the results, it was found that the utilization of solely Sentinel-1 backscatter produced an R^2 of 0.34 while employing only variables from Sentinel-2 resulted in an R^2 of 0.82, and using variables from both satellite images together achieved an R^2 of 0.84. In the study conducted by Güverçin and Günlü (2023a, b) on pure Calabrian pine stands, the relationships between AGB and the reflection values obtained from Sentinel-1 satellite imagery were examined, and, similar to our study, a very low model determination coefficient (0.053) was found. In the same study, the model determination coefficients were 0.313 for Sentinel-1 reflection values with Landsat 8 band reflectance values, 0.292 for vegetation indices, and 0.10 for topographic variables. It was observed that including different variables in the model led to improved model performance. In a study conducted by Keleş et al. (2021), Sentinel-1 (backscatter) and Sentinel-2 (band reflectance and vegetation index) satellite imagery were used to predict aboveground carbon in pure Scotch pine stands. Upon examining the results, the lowest R^2 of 0.442 was obtained in the model where Sentinel-1 backscatter values were used as the independent variable. Additionally, when backscatter variables were included along with band reflectance values, the R^2 increased to 0.634, and when vegetation index values were used, it reached 0.672. In the study conducted by Moghimi et al. (2024) on predicting AGB, the model that included variables derived from both Sentinel-1 and Sentinel-2 imagery demonstrated better performance. Similar results were also found in the study conducted by Wang et al. (2024). The results from the studies indicate that when variables derived from Sentinel-1, ALOS, and other optical satellite imagery are used together, the model performance improves.

Unmanned aerial vehicle

This study also involved modeling the relationships between digital number, band reflectance, vegetation index variables extracted from UAV images, and AGB. Upon evaluating the modeling outcomes, it was found that no significantly correlated model could be formulated using the UAV data, unlike the possibilities achieved with satellite data sources. The R2 ranged between 0.29 for band reflectance and 0.38 for vegetation indices, noticeably lower compared to those derived from satellite data sources (Table 4). However, the UAV data were acquired locally through drone flights over the study area at a considerably lower altitude. This discrepancy might be attributed to the proportional relationship between resolution and the diversity of reflection values. Specifically, when extracting reflection values from 2.5 cm resolution UAV images for the sample areas, the average reflection values encompassed not only reflections from tree canopies but also those from gaps, understory, and the forest floor. Moreover, while a sample area in satellite images might be represented by just a few pixels, the same area in UAV images is depicted by a larger number of pixels, leading to variations in the homogeneity of the sample area data. Consequently, the UAV reflection values do not solely capture data related to dominant trees in the upper tree layer. The reflectance values of objects, such as trees, shrubs, grass, stones, and other elements within the understory and forest floor layers of the forest, are factored into the overall average reflection values of the sampled area. This incorporation of reflection values from the elements in the understory and forest floor layers contributes to increasing the diversity in the average reflection values within the sample area, thereby broadening the dataset's range. This directly affects the model's performance. To overcome the problem, it can be suggested that by utilizing reflection values on an individual tree basis from UAV-acquired images, the standardization of reflection values can be achieved by reducing the number of pixels representing the general sample area, potentially improving the model's performance. In a study conducted by Günlü et al. (2024) in pure Pinus pinaster plantations, reflectance and vegetation index values obtained from UAV imagery captured at a flight altitude of 120 m were used to examine the relationships between various stand parameters, including stand volume, basal area, quadratic mean diameter, dominant height, and number of trees. In the study, reflectance and vegetation index values for the sample areas were calculated using the pixel values of the canopy cover of trees within the sample area, and models were developed. When examining the model performance, significantly higher model results were found compared to our study. The model determination coefficients ranged from 0.40 to 0.83 for reflectance variables, from 0.36 to 0.87 for vegetation index variables, and from 0.39 to 0.86 when both reflectance and vegetation index variables were used together.

Based on the literature review on UAV, it seems that there are a few studies on the estimation of AGB using variables obtained from UAV images, especially in natural forests. In general, these studies focus on the estimation of AGB by evaluating UAV images together with satellite images such as Sentinel-1, Sentinel-2, Landsat 8 and LIDAR. For example, Maesano et al. (2022) in Italy integrated UAV imagery with LIDAR data to estimate AGB using MLR and random forest modeling techniques. Within the scope of the study, a high level of model success was achieved by combining UAV and LIDAR data. In another study by Wang et al. (2020), the AGB was modeled by combining data obtained from UAV-LIDAR and Sentinel-2 imagery with data obtained from ground measurements. It was observed that the model's performance notably improved when the data was assessed collectively.

Literature on the use of UAV data, however, predominantly focuses on estimating AGB with single tree attributes such as diameter and height obtained from UAV images (RGB and NIR bands) or UAV-integrated LIDAR images (Ye et al. 2019; Liu et al. 2022; Lin et al. 2022; Basyuni et al. 2023). However, very few studies focus on the prediction of AGB using band reflectance and vegetation index values obtained from UAV images, as in our study. It becomes evident from the literature that such studies are mostly conducted in agricultural and pasture areas (Niu et al. 2019; Xu et al. 2022; Bazzo et al. 2023), while they are notably scarce in forested areas. For example, Wang et al. (2023) used reflectance and vegetation indices derived from UAV images with various machine learning techniques like Extreme Gradient Boosting (XGBoost), Gradient Boosting Decision Tree (GBDT), Random Forest (RF), Radial Basis Function Neural Network (RBFNN), and Support Vector Regression (SVR) to estimate AGB in Cinnamomum camphora dwarf forests. They indicated that the best relationship between vegetation indices derived from UAV images and AGB was achieved with the XGBoost modeling technique $R^2 = 0.954$), followed by GBDT, RF, RBFNN, and SVR modeling techniques. It was also observed that XGBoost and GBDT modeling techniques resulted in better outcomes for vegetation indices, while RBFNN and SVR modeling techniques yielded better results with band reflectance values. The RF modeling technique resulted in the same outcome for both band reflectance and vegetation indices. In another related study by Anuar et al. (2023), the relationships between UAV-derived NDVI index and AGB were examined in a small local area, revealing moderate relationships ($R^2 = 0.55$). In our study, however, we used UAV with three bands (red, green, and blue) that lacked the NIR band; therefore, numerous indices such as NDVI requiring near-infrared bands were not calculated and were not used as independent variables in the models.

Conclusions

When evaluating the study results, it was observed that the model incorporating texture features from Sentinel-2 satellite imagery using the ANN modeling technique was more successful in predicting AGB. Detailed results obtained from the study are listed below. According to the performance criteria derived from all datasets associated with the MLR;

- When considering different orientations of texture values, the most successful model (0.80) was obtained from Sentinel-2 90°.
- The modeling successes for predicting AGB using vegetation index values were found to be 0.38 for UAV, 0.53 for Landsat 8, and 0.58 for Sentinel-2, respectively.
- The modeling successes for reflectance values and AGB were determined to be 0.29 for UAV, 0.52 for Landsat 8, and 0.47 for Sentinel-2.
- The poorest model results were obtained from the models developed using band brightness (0.03) and backscattering variables (0.07) derived from the Sentinel-1 imagery.

According to the ANN;

- It was found that the most successful model 8 (0.82) was achieved by incorporating texture values from the Sentinel-2 with a 9 × 9 window size as independent variables.

In summary, the model developed using texture variables from Sentinel-2 imagery with ANNs can be applied to similar forest ecosystems (pure Scots pine stands) near the study area.

The study found that the relationships between variables obtained from UAV imagery, which are increasingly used in forestry studies, and AGB were weak. As discussed in the discussion section, the reason for this could be that, due to the high resolution of these images, objects such as stones, grasses, shrubs, etc., located in the lower layers, may affect the reflectance values of the sample areas. Therefore, in future studies involving UAVs, it would be beneficial to consider the reflectance values related to the canopy cover of trees within the sample plots, and in other words, avoid considering the gaps within the sample plot. This could help improve the model performance of the developed models. Likewise, in investigations involving UAVs, the refinement of image acquisition can be achieved by incorporating LIDAR technology into the UAV setup, along with the amalgamation of the variables obtained from these images with ground data, leading to a substantial improvement of models utilized for estimating AGB. However, in future studies aimed at predicting AGB, better model performance could be achieved by incorporating variables obtained from both active and passive satellite imagery into the models. Additionally, by adding other variables, such as topographic variables, and using different modeling techniques like extreme gradient boosting decision trees, deep learning, artificial neural networks, random forests, support vector machines, ensemble methods, and multivariate adaptive regression splines, the model performance can be enhanced.

Acknowledgements This study was produced from a doctoral thesis prepared by Hasan AKSOY and supervised by Prof. Dr. Alkan GÜNLÜ for the Institute of Natural and Applied Science, Çankırı Karatekin University, Türkiye.

Author contributions The writing of the manuscript and creation of the template was carried out by AG, while the generation and analyses of the results were carried out by HA.

Funding This study was funded by the Scientific Research Project Unit of Cankırı Karatekin University (Grant No: OF211221D08).

Data availability No datasets were generated or analysed during the current study.

Declarations

Competing interests The authors declare no competing interests.

11. References

Achard F, Stibig HJ, Eva HD, Lindquist EJ, Bouvet A, Arino O, Mayaux P (2010) Estimating tropical deforestation from Earth observation data. Carbon Manag 1(2):271–287. https://doi.org/10.4155/cmt.10.30

Ahmad N, Ullah S, Zhao N, Mumtaz F, Ali A, Ali A, Shakir M (2023) Comparative analysis of Remote Sensing and Geo-Statistical techniques to Quantify Forest Biomass. Forests 14(2):379. https://doi.org/10.3390/f14020379

Akıllı A, Hülya A (2020) Evaluation of normalization techniques on neural networks for the prediction of 305-day milk yield. Turkish J Agricultural Eng Res 1(2):354–367. https://doi.org/10.46592/turkager.2020.v01i02.011

Alquraish MM, Khadr M (2021) Remote-sensing-based streamflow forecasting using artificial neural network and support vector machine models. Remote Sens 13(20):4147. https://doi.org/10.3390/rs13204147

Anees SA, Mehmood K, Khan WR, Sajjad M, Alahmadi TA, Alharbi SA, Luo M (2024) Integration of machine learning and remote sensing for above ground biomass estimation through Landsat-9 and field data in temperate forests of the himalayan region. Ecol Inf 82:102732. https://doi.org/10.1016/j.ecoinf.2024.102732

Anish KC, Bhattarai S, Pandey P (2022) A comparison of Landsat-8 and Sentinel-2 spectral indices for estimating aboveground forest carbon in a community forest, vol 19. Journal of Institute of Forestry, Forestry, pp 40–55

Anuar NI, Khalid N, Tahar KN, Othman AN (2023), September Analyze the Relationship Between Aboveground Biomass and NDVI Values Derived from UAV Multispectral Imagery. In IOP Conference Series: Earth and Environmental Science (Vol. 1240, No. 1, p. 012015). IOP Publishing

Argamosa RJL, Blanco AC, Baloloy AB, Candido CG, Dumalag JBLC, Dimapilis LLC, Paringit EC (2018) Modelling above ground biomass of mangrove forest using Sentinel-1 imagery. 4:13–20.

Axelsson C, Skidmore AK, Schlerf M, Fauzi A, Verhoef W (2013) Hyperspectral analysis of mangrove foliar chemistry using PLSR and support vector regression. Int J Remote Sens 34(5):1724–1743. https://doi.org/10.1080/01431161.2012.725958

Baloloy AB, Blanco AC, Candido CG, Argamosa RJL, Dumalag JBLC, Dimapilis LLC, Paringit EC (2018) Estimation of mangrove forest aboveground biomass using multispectral bands, vegetation indices and biophysical variables derived from optical satellite imageries: Rapideye, planetscope and sentinel-2. 4:29–36. https://doi.org/10.5194/isprs-annals-IV-3-29-2018

Ban Y, Zhang P, Nascetti A, Bevington AR, Wulder MA (2020) Near real-time wildfire progression monitoring with Sentinel-1 SAR time series and deep learning. Sci Rep 10(1):1322. https://doi.org/10.1038/s41598-019-56967-x

Barbosa JM, Broadbent EN, Bitencourt MD (2014) Remote sensing of aboveground biomass in tropical secondary forests: a review. Int J Forestry Res 2014(1):715796. https://doi.org/10.1155/2014/715796

Basyuni M, Wirasatriya A, Iryanthony SB, Amelia R, Slamet B, Sulistiyono N, Arifanti VB (2023) Aboveground biomass and carbon stock estimation using UAV photogrammetry in Indonesian mangroves and other competing land uses. Ecol Inf 77:102227

Bazzo COG, Kamali B, Hütt C, Bareth G, Gaiser T (2023) A review of estimation methods for aboveground biomass in grasslands using UAV. Remote Sens 15(3):639

Bendig J, Yu K, Aasen H, Bolten A, Bennertz S, Broscheit J, Bareth G (2015) Combining UAV-based plant height from crop surface models, visible, and near infrared vegetation indices for biomass monitoring in barley. Int J Appl Earth Obs Geoinf 39:79–87. https://doi.org/10.1016/j.jag.2015.02.012

Bindu G, Rajan P, Jishnu ES, Joseph KA (2020) Carbon stock assessment of mangroves using remote sensing and geographic information system. Egypt J Remote Sens Space Sci 23(1):1–9. https://doi.org/10.1016/j.ejrs.2018.04.006

Blackburn GA (1998) Spectral indices for estimating photosynthetic pigment concentrations: a test using senescent tree leaves. Int J Remote Sens 19(4):657–675. https://doi.org/10.1080/014311698215919

Bolat F (2021) Ankara Orman Bölge Müdürlüğü Anadolu Karaçamı meşcerelerinde artım ve büyümenin yapay sinir ağları ile modellenmesi. Doktora Tezi (**Çankırı Karatekin Üniversitesi, 193 sayfa, Çankırı**)

Bulut S (2023) Machine learning prediction of above-ground biomass in pure calabrian pine (Pinus brutia Ten.) Stands of the Mediterranean region, Türkiye. Ecol Inf 74:101951. https://doi.org/10.1016/j.ecoinf.2022.101951

Bulut S, Sivrikaya F, Günlü A (2022) Evaluating statistical and combine method to predict stand above-ground biomass using remotely sensed data. Arab J Geosci 15(9):838. https://doi.org/10.1007/s12517-022-10140-3

Bulut S, Günlü A, Çakır G (2023) Modelling some stand parameters using landsat 8 OLI and Sentinel-2 satellite images by machine learning techniques: a case study in Türkiye. Geocarto Int 38(1):2158238

Castillo JAA, Apan AA, Maraseni TN, Salmo III (2017) Estimation and mapping of above-ground biomass of mangrove forests and their replacement land uses in the Philippines using Sentinel imagery. ISPRS J Photogrammetry Remote Sens 134:70–85. https://doi.org/10.1016/j.isprsjprs.2017.10.016

Chen JM (1996) Evaluation of vegetation indices and a modified simple ratio for boreal applications. Can J Remote Sens 22(3):229–242. https://doi.org/10.1080/07038992.1996.10855178

Chen D, Stow DA, Gong P (2004) Examining the effect of spatial resolution and texture window size on classification accuracy: an urban environment case. Int J Remote Sens 25:2177–2192. https://doi.org/10.1080/01431160310001618464

Chen Q, McRoberts RE, Wang C, Radtke PJ (2016) Forest aboveground biomass mapping and estimation across multiple spatial scales using model-based inference. Remote Sens Environ 184:350–360. https://doi.org/10.1016/j.rse.2016.07.023

Chen L, Wang Y, Ren C, Zhang B, Wang Z (2019) Optimal combination of predictors and algorithms for forest above-ground biomass mapping from Sentinel and SRTM data. Remote Sens 11(4):414. https://doi.org/10.3390/rs11040414

Demirel D, Günlü A, Sakıcı OE (2023) Estimating Above-Ground Carbon of Taurus Cedar Stands Using Sentinel-2 Satellite Image: A Case Study of Elmalı Forest Enterprise. In 3rd International Congress on Engineering and Life Science. Trabzon. https://doi.org/10.61326/icelis.2023.45

Dong J, Kaufmann RK, Myneni RB, Tucker CJ, Kauppi PE, Liski J, Hughes MK (2003) Remote sensing estimates of boreal and temperate forest woody biomass: carbon pools, sources, and sinks. Remote Sens Environ 84(3):393–410. https://doi.org/10.1016/S0034-4257(02)00130-X

Dong L, Tang S, Min M, Veroustraete F, Cheng J (2019) Aboveground forest biomass based on OLSR and an ANN model integrating LiDAR and optical data in a mountainous region of China. Int J Remote Sens 40(15):6059–6083. https://doi.org/10.1080/01431161.2019.1587201

Du M, Noguchi N (2017) Monitoring of wheat growth status and mapping of wheat yield's within-field spatial variations using color images acquired from UAV-camera system. Remote Sens 9(3):289. https://doi.org/10.3390/rs9030289

Dube T, Mutanga O (2015) Investigating the robustness of the new Landsat-8 operational land Imager derived texture metrics in estimating plantation forest aboveground biomass in resource constrained areas. ISPRS J Photogrammetry Remote Sens 108:12–32. https://doi.org/10.1016/j.isprsjprs.2015.06.002

Eckert S (2012) Improved forest biomass and carbon estimations using texture measures from WorldView-2 satellite data. Remote Sens 4(4):810–829. https://doi.org/10.3390/rs4040810

Ehlers D, Wang C, Coulston J, Zhang Y, Pavelsky T, Frankenberg E, Song C (2022) Mapping forest aboveground biomass using multisource remotely sensed data. Remote Sens 14(5):1115. https://doi.org/10.3390/rs14051115

El Hage M, Villard L, Huang Y, Ferro-Famil L, Koleck T, Le Toan T, Polidori L (2022) Multicriteria accuracy assessment of digital elevation models (DEMs) produced by airborne P-band polarimetric SAR tomography in tropical rainforests. Remote Sens 14(17):4173. https://doi.org/10.3390/rs14174173

Ercanlı İ, Kurt A, Şenyurt M, Günlü A, Bolat F, Keleş S (2018) Tarsus Yöresi Anadolu Karaçamı Ağaçlarında Hacim Tahminlerinin Yapay Sinir Ağları Ile Elde Edilmesi. Anadolu Orman Araştırmaları Dergisi 4(1):25–37

Foresee FD, Hagan MT (1997), June Gauss-Newton approximation to Bayesian learning. In Proceedings of international conference on neural networks (ICNN'97) (Vol. 3, pp. 1930–1935). IEEE. https://doi.org/10.1109/ICNN.1997.614194

Forkuor G, Dimobe K, Serme I, Tondoh JE (2018) Landsat-8 vs. Sentinel-2: examining the added value of sentinel-2's red-edge bands to land-use and land-cover mapping in Burkina Faso. GIScience Remote Sens 55(3):331–354. https://doi.org/10.1080/15481603.2017.1370169

Gamon JA, Surfus JS (1999) Assessing leaf pigment content and activity with a reflectometer. New Phytol 143(1):105–117

García-Fernández M, Sanz-Ablanedo E, Rodríguez-Pérez JR (2021) High-resolution drone-acquired RGB imagery to estimate spatial grape quality variability. Agronomy 11(4):655. https://doi.org/10.3390/agronomy11040655

Gasparri NI, Parmuchi MG, Bono J, Karszenbaum H, Montenegro CL (2010) Assessing multi-temporal landsat 7 ETM + images for estimating above-ground biomass in subtropical dry forests of Argentina. J Arid Environ 74(10):1262–1270. https://doi.org/10.1016/j.jaridenv.2010.04.007

GDF (2020) Sinop Regional Directorate of Forestry, Forest Planing Unit, Forest Management Plans. Republic of Türkiye. General Directorate of Forestry, Forest Management and Planning Department, Ankara

Georgopoulos N, Sotiropoulos C, Stefanidou A, Gitas IZ (2022) Struct Terrain Forests 13(12):2157. https://doi.org/10.3390/f13122157. Total Stem Biomass Estimation Using Sentinel-1 and-2 Data in a Dense Coniferous Forest of Complex

Gitelson AA, Kaufman YJ, Merzlyak MN (1996) Use of a green channel in remote sensing of global vegetation from EOS-MODIS. Remote Sens Environ 58(3):289–298. https://doi.org/10.1016/S0034-4257(96)00072-7

Gitelson AA, Kaufman YJ, Stark R, Rundquist D (2002) Novel algorithms for remote estimation of vegetation fraction. Remote Sens Environ 80(1):76–87. https://doi.org/10.1016/S0034-4257(01)00289-9

Goel NS, Qin W (1994) Influences of canopy architecture on relationships between various vegetation indices and LAI and FPAR: a computer simulation. Remote Sens Reviews 10(4):309–347. https://doi.org/10.1080/02757259409532252

Günlü A, Ercanli I, Başkent EZ, Çakır G (2014) Estimating aboveground biomass using Landsat TM imagery: A case study of Anatolian Crimean pine forests in Türkiye. Annals For Res 289–298. https://doi.org/10.15287/afr.2014.278

Günlü A, Ercanlı İ, Şenyurt M, Keleş S (2021) Estimation of some stand parameters from textural features from WorldView-2 satellite image using the artificial neural network and multiple regression methods: a case study from Türkiye. Geocarto Int 36(8):918–935. https://doi.org/10.1080/10106049.2019.1629644

Günlü A, Keleş S, Ercanli I, Şenyurt M (2021b) Estimation of above-ground stand carbon using landsat 8 OLI satellite image: A case study from Turkey. Spatial modeling in forest resources management: Rural livelihood and sustainable development, 385–403.https://doi.org/10.1007/978-3-030-56542-816

Günlü A, Bulut S, Aksoy H, Bolat F, Çapar SC (2024) İnsansız Hava Aracı (İHA) Kullanılarak Saf Sahil Çamı (*Pinus pinaster* Ait.) Endüstriyel Plantasyonlarında Ağaçların Tepe Çapı ve Boyu ile Göğüs Yüksekliği Çapları Arasında Fonksiyonel İlişkilerin Kurulması ve Bazı Meşcere Parametrelerinin Modellenmesi. (TÜBİTAK-TOVAG Projesi. (**Proje No: 123O144), Çankırı Karatekin Üniversitesi Orman Fakültesi, Çankırı.**)

Güverçin İ, Günlü A (2023) Saf Kızılçam (Pinus brutia Ten.) Meşcerelerinde Aktif ve Pasif Uydu Görüntüleri Kullanılarak Topraküstü Biyokütlenin Tahmin Edilmesi (Anamur Orman İşletme Şefliği Örneği). Bartın Orman Fakültesi Dergisi 25(1):177–191. https://doi.org/10.24011/barofd.1261299

Güverçin İ, Günlü A (2023) Saf Kızılçam (*Pinus brutia* Ten.) Meşcerelerinde Aktif ve Pasif Uydu Görüntüleri Kullanılarak Toprağüstü Biyokütlenin Tahmin Edilmesi (Anamur Orman İşletme Şefliği Örneği). Bartın Orman Fakültesi Dergisi 25(1):177–191

Hague T, Tillett ND, Wheeler H (2006) Automated crop and weed monitoring in widely spaced cereals. Precision Agric 7:21–32. https://doi.org/10.1007/s11119-005-6787-1

Han H, Wan R, Li B (2021) Estimating forest aboveground biomass using Gaofen-1 images, Sentinel-1 images, and machine learning algorithms: a case study of the Dabie Mountain Region, China. Remote Sens 14(1):176. https://doi.org/10.3390/rs14010176

Herold M, Carter S, Avitabile V, Espejo AB, Jonckheere I, Lucas R, De Sy V (2019) The role and need for space-based forest biomass-related measurements in environmental management and policy. Surv Geophys 40:757–778. https://doi.org/10.1007/s10712-019-09510-6

Huang H, Liu C, Wang X, Zhou X, Gong P (2019) Remote Sens Environ 221:225–234. https://doi.org/10.1016/j.rse.2018.11.017. Integration of multi-resource remotely sensed data and allometric models for forest aboveground biomass estimation in China

Huete AR (1988) A soil-adjusted vegetation index (SAVI). Remote Sens Environ 25(3):295–309. https://doi.org/10.1016/0034-4257(88)90106-X

Hunt ER Jr, Rock BN (1989) Detection of changes in leaf water content using near-and middle-infrared reflectances. Remote Sens Environ 30(1):43–54. https://doi.org/10.1016/0034-4257(89)90046-1

Hunt ER Jr, Doraiswamy PC, McMurtrey JE, Daughtry CS, Perry EM, Akhmedov B (2013) A visible band index for remote sensing leaf chlorophyll content at the canopy scale. Int J Appl Earth Obs Geoinf 21:103–112. https://doi.org/10.1016/j.jag.2012.07.020

Issa S, Dahy B, Saleous N, Ksiksi T (2019) Carbon stock assessment of date palm using remote sensing coupled with field-based measurements in Abu Dhabi (United Arab Emirates). Int J Remote Sens 40(19):7561–7580. https://doi.org/10.1080/01431161.2019.1602795

Jayathunga S, Owari T, Tsuyuki S (2018) The use of fixed–wing UAV photogrammetry with LiDAR DTM to estimate merchantable volume and carbon stock in living biomass over a mixed conifer–broadleaf forest. Int J Appl Earth Obs Geoinf 73:767–777

Jiang Z, Huete AR, Didan K, Miura T (2008) Development of a two-band enhanced vegetation index without a blue band. Remote Sens Environ 112(10):3833–3845. https://doi.org/10.1016/j.rse.2008.06.006

Jiang F, Deng M, Tang J, Fu L, Sun H (2022) Integrating spaceborne LiDAR and Sentinel-2 images to estimate forest aboveground biomass in Northern China. Carbon Balance Manag 17(1):1–13. https://doi.org/10.1186/s13021-022-00212-y

Key CH, Benson NC (2006) Landscape assessment (LA). FIREMON: Fire effects monitoring and inventory system, 164, LA-1

Kumar KK, Nagai M, Witayangkurn A, Kritiyutanant K, Nakamura S (2016) Above ground biomass assessment from combined optical and SAR remote sensing data in Surat Thani Province, Thailand. J Geographic Inform Syst 8(04):506. https://doi.org/10.4236/jgis.2016.84042

Kumar KK, Nagai M, Witayangkurn A, Kritiyutanant K, Nakamura S (2016) Above ground biomass assessment from combined optical and SAR remote sensing data in Surat Thani Province, Thailand. J Geographic Inform Syst 8(4):506–516. https://doi.org/10.4236/jgis.2016.84042

Lan L, Erxue C, Zengyuan L, Qi F, Lei Z (2016) A review on Forest Height and Above\| ground Biomass Estimation based on synthetic aperture radar. Remote Sens Technol Application 31(4):625–633. https://doi.org/10.11873/j.issn.1004-0323.2016.4.0625

Lawrence S, Giles CL, Tsoi AC (1997), July Lessons in neural network training: Overfitting may be harder than expected. In Aaai/iaai (pp. 540–545)

Li B, Wang W, Bai L, Chen N, Wang W (2019) Estimation of aboveground vegetation biomass based on Landsat-8 OLI satellite images in the Guanzhong Basin, China. Int J Remote Sens 40(10):3927–3947. https://doi.org/10.1080/01431161.2018.1553323

Li Y, Li C, Li M, Liu Z (2019) Influence of variable selection and forest type on forest aboveground biomass estimation using machine learning algorithms. Forests 10:1073. https://doi.org/10.3390/f10121073

Li Y, Li M, Li C, Liu Z (2020) Forest aboveground biomass estimation using landsat 8 and Sentinel-1A data with machine learning algorithms. Sci Rep 10(1):9952. https://doi.org/10.1038/s41598-020-67024-3

Li C, Zhou L, Xu W (2021) Estimating aboveground biomass using Sentinel-2 MSI data and ensemble algorithms for grassland in the Shengjin Lake Wetland, China. Remote Sens 13(8):1595. https://doi.org/10.3390/rs13081595

Lin J, Chen D, Wu W, Liao X (2022) Estimating aboveground biomass of urban forest trees with dual-source UAV acquired point clouds. Urban Forestry Urban Green 69:127521. https://doi.org/10.1016/j.ufug.2022.127521

Listopad CM, Drake JB, Masters RE, Weishampel JF (2011) Portable and airborne small footprint LiDAR: forest canopy structure estimation of fire managed plots. Remote Sens 3(7):1284–1307. https://doi.org/10.3390/rs3071284

Liu HQ, Huete A (1995) A feedback based modification of the NDVI to minimize canopy background and atmospheric noise. IEEE Trans Geosci Remote Sens 33(2):457–465

Liu Y, Feng H, Yue J, Fan Y, Jin X, Song X, Yang G (2022) Estimation of Potato above-ground Biomass based on Vegetation indices and Green-Edge parameters obtained from UAVs. Remote Sens 14(21):5323

López-Serrano PM, López-Sánchez CA, Álvarez-González JG, García-Gutiérrez J (2016) A comparison of machine learning techniques applied to Landsat-5 TM spectral data for biomass estimation. Can J Remote Sens 42(6):690–705. https://doi.org/10.1080/07038992.2016.1217485

Louhaichi M, Borman MM, Johnson DE (2001) Spatially located platform and aerial photography for documentation of grazing impacts on wheat. Geocarto Int 16(1):65–70. https://doi.org/10.1080/10106040108542184

Lu D (2005) Aboveground biomass estimation using landsat TM data in the Brazilian Amazon. Int J Remote Sens 26(12):2509–2525. https://doi.org/10.1080/01431160500142145

Lu D, Chen Q, Wang G, Moran E, Batistella M, Zhang M, Saah D (2012) Aboveground forest biomass estimation with Landsat and LiDAR data and uncertainty analysis of the estimates. International Journal of Forestry Research, 2012. https://doi.org/10.1155/2012/436537

Maack J, Kattenborn T, Fassnacht FE, Enßle F, Hernandez J, Corvalan P, Koch B (2015) Modeling forest biomass using very-high-resolution data—combining textural, spectral and photogrammetric predictors derived from spaceborne stereo images. Eur J Remote Sens 48(1):245–261. https://doi.org/10.5721/EuJRS20154814

Maesano M, Santopuoli G, Moresi FV, Matteucci G, Lasserre B, Mugnozza S (2022) Above ground biomass estimation from UAV high resolution RGB images and LiDAR data in a pine forest in Southern Italy. iForest-Biogeosciences Forestry 15(6):451

Mauya EW, Madundo S (2021) Modelling and Mapping Above Ground Biomass Using Sentinel 2 and Planet Scope Remotely Sensed Data in West Usambara Tropical Rainforests, Tanzania. . https://doi.org/10.21203/rs.3.rs-942337/v1

McFeeters SK (1996) The use of the normalized difference Water Index (NDWI) in the delineation of open water features. Int J Remote Sens 17(7):1425–1432. https://doi.org/10.1080/01431169608948714

Moghimi A, Darestani AT, Mostofi N, Fathi M, Amani M (2024) Improving forest above-ground biomass estimation using genetic-based feature selection from Sentinel-1 and Sentinel-2 data (case study of the Noor forest area in Iran). Kuwait J Sci 51(2):100159. https://doi.org/10.1016/j.kjs.2023.11.008

Moradi F, Sadeghi SMM, Heidarlou HB, Deljouei A, Boshkar E, Borz SA (2022) Above-ground biomass estimation in a Mediterranean sparse coppice oak forest using Sentinel-2 data. Annals for Res 65(1):165–182. https://doi.org/10.15287/afr.2022.2390

Muhe S, Argaw M (2022) Estimation of above-ground biomass in tropical afro-montane forest using Sentinel-2 derived indices. Environ Syst Res 11(1):1–22. https://doi.org/10.1186/s40068-022-00250-y

Nasirzadehdizaji R, Balik Sanli F, Abdikan S, Cakir Z, Sekertekin A, Ustuner M (2019) Sensitivity analysis of multi-temporal Sentinel-1 SAR parameters to crop height and canopy coverage. Appl Sci 9(4):655. https://doi.org/10.3390/app9040655

Nguyen TP, Nguyen PK, Nguyen HN, Tran TD, Pham GT, Le TH, Nguyen VB (2024) Evaluation of statistical and machine learning models using satellite data to estimate aboveground biomass: A study in Vietnam Tropical Forests. For Sci Technol 1–13. https://doi.org/10.1080/21580103.2024.2409211

Ni W, Dong J, Sun G, Zhang Z, Pang Y, Tian X, Chen E (2019) Synthesis of leaf-on and leaf-off unmanned aerial vehicle (UAV) stereo imagery for the inventory of aboveground biomass of deciduous forests. Remote Sens 11(7):889. https://doi.org/10.3390/rs11070889

Niu Y, Zhang L, Zhang H, Han W, Peng X (2019) Estimating above-ground biomass of maize using features derived from UAV-based RGB imagery. Remote Sens 11(11):1261

Nuthammachot N, Askar A, Stratoulias D, Wicaksono P (2022) Geocarto Int 37(2):366–376. https://doi.org/10.1080/10106049.2020.1726507. Combined use of Sentinel-1 and Sentinel-2 data for improving above-ground biomass estimation

Okut H (2016) Bayesian regularized neural networks for small n big p data. Artif Neural networks-models Appl. https://doi.org/10.5772/63256

Ou G, Li C, Lv Y, Wei A, Xiong H, Xu H, Wang G (2019) Improving aboveground biomass estimation of Pinus densata forests in Yunnan using landsat 8 imagery by incorporating age dummy variable and method comparison. Remote Sens 11(7):738. https://doi.org/10.3390/rs11070738

Ouchi K (2013) Recent trend and advance of synthetic aperture radar with selected topics. Remote Sens 5(2):716–807. https://doi.org/10.3390/rs5020716

Özdemir G (2018) Karabük Yöresi Kayın-Göknar Karışık Meşcerelerinde Gövde Çaplarının Yapay Sinir Ağları ile Tahmin Edilmesi, Kastamonu Üniversitesi, Fen Bilimleri Enstitüsü, Orman Mühendisliği Ana Bilimdalı Yüksek Lisans Tezi, 101 s

Persson HJ (2016) Estimation of Boreal forest attributes from very high-resolution pleiades data. Remote Sens 8(9):736. https://doi.org/10.3390/rs8090736

Pham TD, Yokoya N, Bui DT, Yoshino K, Friess DA (2019) Remote sensing approaches for monitoring mangrove species, structure, and biomass: opportunities and challenges. Remote Sens 11(3):230. https://doi.org/10.3390/rs11030230

Phua MH, Johari SA, Wong OC, Ioki K, Mahali M, Nilus R, Hashim M (2017) Synergistic use of Landsat 8 OLI image and airborne LiDAR data for above-ground biomass estimation in tropical lowland rainforests. For Ecol Manag 406:163–171. https://doi.org/10.1016/j.foreco.2017.10.007

Piotrowski AP, Napiorkowski JJ (2013) A comparison of methods to avoid overfitting in neural networks training in the case of catchment runoff modelling. J Hydrol 476:97–111. https://doi.org/10.1016/j.jhydrol.2012.10.019

PIX4D (2022) https://www.pix4d.com/product/pix4dmapper-photogrammetry-software/

Poudel KP, Cao QV (2013) Evaluation of methods to predict Weibull parameters for characterizing diameter distributions. For Sci 59(2):243–252. https://doi.org/10.5849/forsci.12-001

Puliti S, Breidenbach J, Schumacher J, Hauglin M, Klingenberg TF, Astrup R (2021) Above-ground biomass change estimation using national forest inventory data with Sentinel-2 and Landsat. Remote sensing of environment, 265, 112644. https://doi.org/10.1016/j.rse.2021.112644

Quang NH, Quinn CH, Carrie R, Stringer LC, Hackney CR, Van Tan D (2022) Comparisons of regression and machine learning methods for estimating mangrove above-ground biomass using multiple remote sensing data in the Red River estuaries of Vietnam. Remote Sens Applications: Soc Environ 26:100725. https://doi.org/10.1016/j.rsase.2022.100725

Quegan S, Le Toan T, Chave J, Dall J, Exbrayat JF, Minh DHT, Williams M (2019) The European Space Agency BIOMASS mission: measuring forest above-ground biomass from space. Remote Sens Environ 227:44–60. https://doi.org/10.1016/j.rse.2019.03.032

Ronoud G, Fatehi P, Darvishsefat AA, Tomppo E, Praks J, Schaepman ME (2021) Multi-sensor aboveground biomass estimation in the broadleaved Hyrcanian forest of Iran. Can J Remote Sens 47(6):818–834. https://doi.org/10.1080/07038992.2021.1968811

Rouse JW, Haas RH, Schell JA, Deering DW (1974) Monitoring vegetation systems in the Great Plains with ERTS. NASA Spec Publ 351(1):309

Safari A, Sohrabi H, Powell S, Shataee S (2017) A comparative assessment of multi-temporal landsat 8 and machine learning algorithms for estimating aboveground carbon stock in coppice oak forests. Int J Remote Sens 38(22):6407–6432. https://doi.org/10.1080/01431161.2017.1356488

Sakici OE, Gunlu A (2018) Artificial intelligence applications for predicting some stand attributes using Landsat 8 OLI satellite data: A case study from Turkey

Santoro M, Cartus O, Carvalhais N, Rozendaal D, Avitabilie V, Araza A, Willcock S (2020) The global forest above-ground biomass pool for 2010 estimated from high-resolution satellite observations. Earth Syst Sci Data Discuss 2020:1–38. https://doi.org/10.5194/essd-13-3927-2021

Sarker LR, Nichol JE (2011) Improved forest biomass estimates using ALOS AVNIR-2 texture indices. Remote Sens Environ 115:968–977. https://doi.org/10.1016/j.rse.2010.11.010

Sibanda M, Mutanga O, Rouget M, Kumar L (2017) Estimating biomass of native grass grown under complex management treatments using Worldview-3 spectral derivatives. Remote Sens 9:55. https://doi.org/10.3390/rs9010055

Silva CA, Saatchi S, Garcia M, Labriere N, Klauberg C, Ferraz A, Hudak AT (2018) Comparison of small-and large-footprint lidar characterization of tropical forest aboveground structure and biomass: a case study from Central Gabon. IEEE J Sel Top Appl Earth Observations Remote Sens 11(10):3512–3526

Sivasankar T, Lone JM, Sarma KK, Qadir° A, Raju PLN (2013) Estimation of above ground biomass using support vector. Vietnam J Earth Sci 41(2):95–104

Skudnik M, Jevšenak J (2022) Artificial neural networks as an alternative method to nonlinear mixed-effects models for tree height predictions. For Ecol Manag 507:120017. https://doi.org/10.1016/j.foreco.2022.120017

Soja MJ, Persson HJ, Ulander LM (2015) Estimation of forest biomass from two-level model inversion of single-pass InSAR data. IEEE Trans Geosci Remote Sens 53(9):5083–5099

Tang J, Liu Y, Li L, Liu Y, Wu Y, Xu H, Ou G (2022) Enhancing Aboveground Biomass Estimation for three Pinus forests in Yunnan, SW China, using landsat 8. Remote Sens 14(18):4589. https://doi.org/10.3390/rs14184589

Tao Y, ZHANG YM (2013) Multi-scale biomass estimation of desert shrubs: a case study of Haloxylon Ammodendron in the Gurbantunggut Desert, China. Acta Prataculturae Sinica 22(6):1

Thapa RB, Watanabe M, Motohka T, Shimada M (2015) Potential of high-resolution ALOS–PALSAR mosaic texture for aboveground forest carbon tracking in tropical region. Remote Sens Environ 160:122–133. https://doi.org/10.1016/j.rse.2015.01.007

Themistocleous K (2019), June DEM modeling using RGB-based vegetation indices from UAV images. In Seventh International Conference on Remote Sensing and Geoinformation of the

Environment (RSCy2019) (Vol. 11174, pp. 499–506). SPIE. https://doi.org/10.1117/12.2532748
Tucker CJ (1979) Red and photographic infrared linear combinations for monitoring vegetation. Remote Sens Environ 8(2):127–150. https://doi.org/10.1016/0034-4257(79)90013-0
Tucker CJ (1980) A spectral method for determining the percentage of green herbage material in clipped samples. Remote Sens Environ 9(2):175–181. https://doi.org/10.1016/0034-4257(80)90007-3
Turgut R, Günlü A (2022) Estimating aboveground biomass using landsat 8 satellite image in pure Crimean pine (Pinus nigra JF Arnold subsp. pallasiana (Lamb.) Holmboe) stands: a case from Türkiye. Geocarto Int 37(3):720–734. https://doi.org/10.1080/10106049.2020.1737971
Vashum KT, Jayakumar S (2012) Methods to estimate above-ground biomass and carbon stock in natural forests-a review. J Ecosyst Ecography 2(4):1–7. https://doi.org/10.4172/2157-7625.1000116
Wan R, Wang P, Wang X, Yao X, Dai X (2018) Modeling wetland aboveground biomass in the Poyang Lake National Nature Reserve using machine learning algorithms and Landsat-8 imagery. J Appl Remote Sens 12:1–16. https://doi.org/10.1117/1.JRS.12.046029
Wang J, Xiao X, Bajgain R, Starks P, Steiner J, Doughty RB, Chang Q (2019) Estimating leaf area index and aboveground biomass of grazing pastures using Sentinel-1, Sentinel-2 and Landsat images. ISPRS J Photogrammetry Remote Sens 154:189–201. https://doi.org/10.1016/j.isprsjprs.2019.06.007
Wang D, Wan B, Liu J, Su Y, Guo Q, Qiu P, Wu X (2020) Estimating aboveground biomass of the mangrove forests on northeast Hainan Island in China using an upscaling method from field plots, UAV-LiDAR data and Sentinel-2 imagery. Int J Appl Earth Obs Geoinf 85:101986. https://doi.org/10.1016/j.jag.2019.101986
Wang S, Wang D, Sun JR (2022) Artificial neural network-based ionospheric delay correction method for satellite-based augmentation systems. Remote Sens 14:676
Wang Q, Lu X, Zhang H, Yang B, Gong R, Zhang J, Zhao J (2023) Comparison of machine learning methods for estimating Leaf Area Index and Aboveground Biomass of Cinnamomum camphora based on UAV Multispectral Remote Sensing Data. Forests 14(8):1688
Wang C, Zhang W, Ji Y, Marino A, Li C, Wang L, Wang M, Forests (2024) 15(1), 215. https://doi.org/10.3390/f15010215
Woebbecke DM, Meyer GE, Von Bargen K, Mortensen DA (1995) Shape features for identifying young weeds using image analysis. Trans ASAE 38(1):271–281
Xu X, Du H, Zhou G, Ge H, Shi Y, Zhou Y, Fan W, Fan W (2011) Estimation of aboveground carbon stock of Moso bamboo (Phyllostachysheterocycla var. Pubescens) forest with a Landsat Thematic Mapper image. Int J Remote Sens 32(5):1431–1448. https://doi.org/10.1080/01431160903551389
Xu T, Wang F, Xie L, Yao X, Zheng J, Li J, Chen S (2022) Integrating the textural and spectral information of uav hyperspectral images for the improved estimation of rice aboveground biomass. Remote Sens 14(11):2534
Yadav S, Padalia H, Sinha SK, Srinet R, Chauhan P (2021) Above-ground biomass estimation of Indian tropical forests using X band Pol-InSAR and Random Forest. Remote Sens Applications: Soc Environ 21:100462. https://doi.org/10.1016/j.rsase.2020.100462
Yavaşli DD, Ölgen MK (2017) Modeling above Ground Biomass in calabrian Pine forests of Düzlerçami (Antalya). Ege Coğrafya Dergisi 26(2):151–161
Yavuz H, Mısır N, Tüfekçioğlu A, Altun L, Mısır M, Ercanlı İ, Sakıcı OE, Kahriman A, Karahalil U, Yılmaz M, Sarıyıldız T, Küçük M, Meydan G, Bayburtlu Ş, Bilgili F, Aydın AC, Kara Ö, Bolat İ ve, Usta A 2010. Karadeniz Bölgesi saf ve karışık Sarıçam (Pinus slyvestris L.) meşcereleri için mekanistik büyüme modellerinin geliştirilmesi, biyokütle ve karbon depolama miktarlarının belirlenmesi. (TÜBİTAK-TOVAG Projesi, Proje No: 106O274), Karadeniz Teknik Üniversitesi Orman Fakültesi, Trabzon
Ye N, van Leeuwen L, Nyktas P (2019) Analysing the potential of UAV point cloud as input in quantitative structure modelling for assessment of woody biomass of single trees. Int J Appl Earth Obs Geoinf 81:47–57. https://doi.org/10.1016/j.jag.2019.05.010
Zarco-Tejada PJ, Berjón A, López-Lozano R, Miller JR, Martín P, Cachorro V, De Frutos A (2005) Assessing vineyard condition with hyperspectral indices: Leaf and canopy reflectance simulation in a row-structured discontinuous canopy. Remote Sens Environ 99(3):271–287. https://doi.org/10.1016/j.rse.2005.09.002
Zhang L, Shao Z, Diao C (2015) Synergistic retrieval model of forest biomass using the integration of optical and microwave remote sensing. J Appl Remote Sens 9(1):096069–096069. https://doi.org/10.1117/1.JRS.9.096069
Zhang C, Denka S, Cooper H, Mishra DR (2018) Quantification of sawgrass marsh aboveground biomass in the coastal Everglades using object-based ensemble analysis and landsat data. Remote Sens Environ 204:366–379. https://doi.org/10.1016/j.rse.2017.10.018
Zhang C, Huang C, Li H, Liu Q, Li J, Bridhikitti A, Liu G (2020) Effect of Textural features in Remote Sensed Data on Rubber Plantation extraction at different levels of spatial resolution. Forests 11:399. https://doi.org/10.3390/f11040399
Zhang W, Zhao L, Li Y, Shi J, Yan M, Ji Y (2022) Forest above-Ground Biomass Inversion Using Optical and SAR images based on a Multi-step Feature Optimized Inversion Model. Remote Sens 14(7):1608. https://doi.org/10.3390/rs14071608
Zhang X, Li L, Liu Y, Wu Y, Tang J, Xu W, Ou G (2023) Improving the accuracy of forest aboveground biomass using landsat 8 images by quantile regression neural network for Pinus densata forests in southwestern China. Front Forests Global Change 6:1162291. https://doi.org/10.3389/ffgc.2023.1162291
Zhang L, Zhao Y, Chen C, Li X, Mao F, Lv L, Du H (2024) UAV-LiDAR Integration with Sentinel-2 enhances Precision in AGB estimation for bamboo forests. Remote Sens 16(4):705. https://doi.org/10.3390/rs16040705
Zhao P, Masoumi Z, Kalantari M, Aflaki M, Mansourian A (2022) A GIS-based landslide susceptibility mapping and variable importance analysis using artificial intelligent training-based methods. Remote Sens 14(1):211. https://doi.org/10.3390/rs14010211
Zheng D, Rademacher J, Chen J, Crow T, Bresee M, Le Moine J, Ryu SR (2004) Estimating aboveground biomass using landsat 7 ETM + data across a managed landscape in northern Wisconsin. USA Remote Sens Environ 93(3):402–411. https://doi.org/10.1016/j.rse.2004.08.008
Zhou J, Guo RY, Sun M, Di TT, Wang S, Zhai J, Zhao Z (2017) The effects of GLCM parameters on LAI estimation using texture values from Quickbird Satellite Imagery. Sci Rep 7(1):1–12. https://doi.org/10.1038/s41598-017-07951-w
Zhu J, Huang Z, Sun H, Wang G (2017) Mapping forest ecosystem biomass density for Xiangjiang River Basin by combining plot and remote sensing data and comparing spatial extrapolation methods. Remote Sens 9(3):241. https://doi.org/10.3390/rs9030241